Research Square

Preprints are preliminary reports that have not undergone peer review.
They should not be considered conclusive, used to inform clinical practice,
or referenced by the media as validated information.

Spectral and Time-Domain Analysis of Nonlinear Irregular Waves on Tubular Offshore Structures: Theory and Extreme Statistics

Leonardo Sant'Anna do Nascimento

leotubi15@hotmail.com

Research Article

Keywords:

Posted Date: November 17th, 2026

DOI: https://doi.org/10.21203/rs.3.rs-11756269/v1

License: This work is licensed under a Creative Commons Attribution 4.0 International License.
Read Full License

Additional Declarations: No competing interests reported.

Spectral and Time-Domain Analysis of Nonlinear Irregular Waves on Tubular Offshore Structures: Theory and Extreme Statistics

Leonardo Sant'Anna do Nascimento

Corresponding author(s). E-mail(s): leotubi15@hotmail.com;

Abstract

This paper aims to consolidate the physical, numerical, and statistical framework for second-order irregular waves and dynamic response, with emphasis on a published shallow-water wind-tower case study. Each governing equation is introduced with its physical purpose, assumptions, and role in the environmental-to-response numerical procedure. A comprehensive wave theory, Morison loading, finite-element dynamics, implicit and explicit integration, non-Gaussian statistics, extreme-value models, verification requirements, and reproducibility practices are included. The tower geometry and analysis numerical procedure are reconstructed from the published model data. The paper examines the reported conclusion that neglect of nonlinear free-surface effects may underestimate short-term response parameters, while distinguishing case evidence from universal design rules.

Keywords: nonlinear irregular waves; second-order potential theory; tubular structures; offshore wind tower; Morison equation; extreme response; L-moments; Newmark method

Nomenclature and abbreviations

Abbreviations

CDF	cumulative distribution function
DOF	degree of freedom
FE/FEA	finite element/finite-element analysis
FFT/IFFT	fast Fourier transform/inverse fast Fourier transform
FRF	frequency response function

GEV	generalized extreme-value distribution
GPD	generalized Pareto distribution
HHT-α	Hilber–Hughes–Taylor time-integration method
JONSWAP	Joint North Sea Wave Project spectrum
L-moment	linear moment based on order statistics
PM	Pierson–Moskowitz spectrum
POT	peaks over threshold
QTF	quadratic transfer function
RK4	fourth-order Runge–Kutta method
SLS/ULS	serviceability/ultimate limit state

Roman symbols

a_i	amplitude of wave component i
a_N, b_N	Gumbel normalizing constants for the maximum of N variables
A	displaced cross-sectional area; system matrix when defined locally
A_e, E, I_e, L_e	element area, Young modulus, second moment of area, and length
C_A, C_D, C_M	added-mass, drag, and inertia coefficients
$C_X(\tau)$	autocovariance function of process X
D, t	external diameter and wall thickness
$E[\cdot]$	expectation operator
F_X, f_X	cumulative distribution and probability-density functions
g	gravitational acceleration
$G(x)$	GEV cumulative distribution
h	still-water depth
H_s, H_{m0}	significant and spectral significant wave heights
$H(y)$	generalized Pareto excess distribution
k, k_i	wavenumber and component wavenumber
KC	Keulegan–Carpenter number
$\mathbf{K}, \mathbf{C}, \mathbf{M}$	global stiffness, damping, and mass matrices
m_j	spectral moment of order j
M_b, V_b	bending moment and base shear
N, N_p	number of harmonics and number of peaks
p	hydrodynamic pressure
$q_r, \boldsymbol{q}$	modal coordinate and modal-coordinate vector
Q_{ij}^+, Q_{ij}^-	sum- and difference-frequency QTFs
Re	Reynolds number
S_η, S_X	one-sided elevation and response spectra
$\mathbf{S}_{XX}(\omega)$	cross-spectral (spectral density) matrix of the process $\boldsymbol{X}(t)$
$t, \Delta t, T$	time, time step, and record duration
T_p, T_z, T_n	spectral peak, zero-crossing, and natural periods
$u, w, \dot{u}$	horizontal velocity, vertical velocity, and horizontal acceleration
U, U_c	wind/reference velocity and current velocity
Ur	Ursell number

$X(t,\vartheta)$	real-valued stochastic process; the outcome ϑ selects one realization
$\boldsymbol{x}, \dot{\boldsymbol{x}}, \ddot{\boldsymbol{x}}$	displacement, velocity, and acceleration vectors
$x_{\max}, x_{\text{ext}}$	sample maximum and inferred extreme response
z	vertical coordinate positive upward
Greek symbols and operators	
$\Omega_s, \mathcal{F}, \mathbb{P}$	sample space, event σ-algebra, and probability measure
α, β, γ	distribution, spectrum, or integration parameters as defined locally
β_r	probability-weighted moment of order r
γ_1, γ_2	skewness and kurtosis
δ_R	relative convergence change in response R
ϵ	perturbation parameter or numerical tolerance
ε_i	random phase of component i
$\eta, \eta^{(1)}, \eta^{(2)}$	total, first-order, and second-order surface elevation
θ	model-parameter vector
ϑ	outcome (element) of the sample space Ω_s
λ_r, τ_r	L-moment and L-moment ratio
μ, σ, ξ	location, scale, and shape parameters
ν	kinematic viscosity or crossing rate as defined locally
ρ	fluid density
$\Phi, \Phi^{(1)}, \Phi^{(2)}$	total, first-order, and second-order velocity potentials
$\boldsymbol{\Psi}, \boldsymbol{\phi}_r$	modal matrix and eigenvector of mode r
$\omega, \omega_p, \omega_r$	angular, spectral-peak, and natural angular frequencies
ζ_r	modal damping ratio
∇, ∇^2	gradient and Laplacian operators
$\|\cdot\|_2$	Euclidean norm

Integrated physical and mathematical framework

The analysis of tubular offshore structures under irregular environmental loading is intrinsically multidisciplinary [10, 13, 16]; the environmental description is stochastic; the wave field is governed by a boundary-value problem, loading is nonlinear through drag and wet-surface variation, and structural response is filtered by inertia, damping, and stiffness. The governing equations are therefore presented in the order in which information passes through the idealized model.

Linear random-wave theory remains the essential reference because it establishes spectral variance, finite-depth dispersion, and Gaussian benchmarks. Its limitation in shallow water is physical rather than merely statistical: symmetric harmonic components cannot reproduce crest-trough asymmetry generated by the nonlinear free-surface conditions. The second-order potential solution of Sharma and Dean introduces bound interactions while retaining a computationally tractable spectral representation [45].

The structural problem adds a second nonlinearity even when material and geometry remain linear. Morison drag is quadratic in relative velocity, so Gaussian kinematics

need not produce Gaussian force [13, 28, 39]. Partial submergence also makes the load profiles time dependent. These mechanisms explain why response skewness, peak distributions, and most-probable extremes require explicit scrutiny rather than automatic use of Gaussian closed forms.

A time-domain formulation is adopted because second-order wave components, current, turbulent wind, wet-length variation, and drag can be retained without equivalent-linearization assumptions. The consistent finite-element formulation transforms distributed loading into nodal forces, while Newmark, HHT-α, or RK4 advances the equilibrium solution in time [5, 22, 29].

The statistical assessment completes the engineering numerical procedure. Conventional moments, L-moments, crossing theory, translation models, Weibull estimators, block maxima, and POT models describe different stochastic objects [24, 37, 46, 47]. The reported numerical investigation indicates that neglecting shallow-water nonlinearity may underestimate response parameters relevant to ULS and fatigue and that peak-adaptive models can improve extreme estimates, although with estimator variability [42].

1 Introduction

1.1 Background and engineering motivation

Offshore towers, piles, jack-up legs, monopiles, conductors, and other slender structural systems are subjected to environmental actions that vary over a broad range of temporal and spatial scales. Wind, waves, and current are not deterministic load histories. They are uncertain fields whose statistics depend on climate, water depth, storm evolution, directionality, and the response bandwidth of the structure. A defensible analysis must therefore preserve the numerical procedure from environmental description to structural response and from short-term response to extreme-value inference.

The central difficulty is coupling: wave elevation determines particle velocity and acceleration; these kinematic quantities generate drag and inertia; structural motion changes relative velocity; the resulting nonlinear force excites a structure whose modal properties feed back into the load. The statistical distribution of response is consequently not implied by the wave spectrum alone. Quadratic drag, intermittent wetting, second-order wave terms, and modal filtering may produce skewness, excess kurtosis, and serially dependent peaks.

1.2 Scope and contribution

The study provides a sequential theoretical formulation consistent with the capabilities represented in the computational framework. The contribution is a traceable hierarchy of equations, assumptions, discretizations, estimators, and verification checks. The intended use is research-grade simulation and methodological assessment, not direct certification of a design without site-specific calibration and validation.

1.3 Organization

The paper proceeds from probability and spectral theory to wave and wind models, nonlinear kinematics, hydrodynamic and aerodynamic loads, finite elements, modal analysis, time integration, statistics of peaks and extremes, uncertainty, and verifications.

2 Random-Process and Spectral Foundations

2.1 Probability space and stochastic processes

Let $(\Omega_s, \mathcal{F}, \mathbb{P})$ be the probability space and let $X(t, \vartheta)$ be a real-valued process, where $\vartheta \in \Omega_s$ denotes an outcome. The mean, autocovariance, and autocorrelation are

$$\mu_X(t) = \mathbb{E}[X(t)], \tag{1}$$

$$C_X(t_1, t_2) = \mathbb{E}[(X(t_1) - \mu_X(t_1))(X(t_2) - \mu_X(t_2))], \tag{2}$$

$$\rho_X(t_1, t_2) = \frac{C_X(t_1, t_2)}{\sigma_X(t_1)\sigma_X(t_2)}. \tag{3}$$

Wide-sense stationarity requires constant mean and covariance dependent only on lag $\tau = t_2 - t_1$. Ergodicity, the property that time averages from a single sufficiently long record converge to ensemble averages, is an additional property and must not be assumed merely because a process is stationary. In practical simulation, ensemble moments are often estimated from finite records; this substitution is justified only when record length is large enough relative to the integral correlation time.

The probability space $(\Omega_s, \mathcal{F}, \mathbb{P})$ is the mathematical stage on which randomness is defined: each outcome ϑ selects one complete realization of the sea surface or structural response, and the measure $\mathbb{P}$ assigns probabilities to events. In plain terms, it replaces the vague idea of "random waves" with a precise object whose averages can be computed. This foundation is needed because every quantity downstream, spectra, response variances, exceedance probabilities, is defined as an expectation over this space. The distinction between ensemble and time averages, central to the ergodicity discussion, is developed in [57, 110]. Kolmogorov's 1933 axiomatization made this abstraction rigorous, and it is worth remembering that every realization in the numerical procedure is, formally, one point ϑ in this space [133]. The practical consequence is that convergence of sample statistics with record length is convergence in this measure-theoretic sense, which is why the paper's verification tests check moments against theory before trusting extremes.

2.2 Spectral density and Fourier pair

The spectral density $S_X(\omega)$ answers the question: how much of the process variance lives at each frequency? The Wiener–Khinchin pair translates the time-domain memory of the process (its autocovariance) into a frequency-domain energy distribution, and back. Intuitively, a narrow tall spectrum means nearly sinusoidal motion; a broad

flat one means noisy, irregular motion. In the numerical chain, the spectrum is the single input from which wave kinematics, structural response, and fatigue damage are all derived, so its definition must be exact—including the one-sided versus two-sided convention. The theory is classical: [51, 103, 110], with the oceanographic viewpoint in [23, 34]. A common pitfall worth stressing is the factor of two between one-sided and two-sided conventions: the paper adopts the one-sided ocean-engineering convention throughout, so that integrating $S_X(\omega)$ over positive frequencies recovers the variance exactly. Any comparison with structural-dynamics literature, which often uses two-sided spectra, must convert explicitly [8, 103].

For a stationary process, the Wiener–Khinchin relation [51] connects covariance and the two-sided spectrum,

$$C_X(\tau) = \frac{1}{2\pi}\int_{-\infty}^{\infty} S_X^{(2)}(\omega)e^{\mathrm{i}\omega\tau}\mathrm{d}\omega, \qquad S_X^{(2)}(\omega) = \int_{-\infty}^{\infty} C_X(\tau)e^{-\mathrm{i}\omega\tau}\mathrm{d}\tau. \tag{4}$$

For a real process, $S_X^{(2)}(-\omega) = S_X^{(2)}(\omega)$. The one-sided density used in ocean engineering satisfies $S_X(\omega) = 2S_X^{(2)}(\omega)$ for $\omega > 0$ and

$$\sigma_X^2 = m_0 = \int_0^{\infty} S_X(\omega)\mathrm{d}\omega. \tag{5}$$

Confusion between one-sided and two-sided conventions may cause a factor-of-two error in amplitudes and a factor-of-four error in quadratic load variance.

2.3 Spectral moments, bandwidth, and crossings

Spectral moments $m_n = \int_0^{\infty} \omega^n S(\omega)\, d\omega$ compress the whole spectrum into a few numbers: m_0 is the variance, m_2 governs the mean zero-crossing rate, m_4 the mean rate of maxima. The bandwidth parameter ε measures how "groupy" or regular the sea is, which controls whether peaks follow a Rayleigh law or something broader. These moments are needed because Rice's crossing theory is written entirely in terms of m_0, m_2, and m_4. The classical derivations are in [6, 26, 37], with modern exposition in [102, 124]. In practice m_4 is the most delicate moment because the ω^4 weight amplifies the high-frequency tail, where the spectrum is least certain; this is one reason the paper favors robust estimators downstream. The bandwidth parameter $\varepsilon = \sqrt{1 - m_2^2/(m_0 m_4)}$ then quantifies how far the sea departs from the narrow-band ideal [6].

The moments

$$m_j = \int_0^{\infty} \omega^j S_X(\omega)\mathrm{d}\omega \tag{6}$$

define characteristic rates and periods. For sufficiently smooth Gaussian processes,

$$\nu_0^+ = \frac{1}{2\pi}\sqrt{\frac{m_2}{m_0}}, \qquad \nu_p = \frac{1}{2\pi}\sqrt{\frac{m_4}{m_2}}, \qquad \epsilon = \sqrt{1 - \frac{m_2^2}{m_0 m_4}}. \tag{7}$$

The parameter ϵ approaches zero for a narrow-band process and increases as the spectrum broadens. Since differentiation weights high frequency, m_4 is sensitive to truncation, noise, and an inadequate upper cutoff.

2.4 Cross-spectral matrices

When several quantities vary together—wave elevation at two points, or wind at several heights—the cross-spectral matrix $S_{ij}(\omega)$ records both their individual spectra (diagonal) and their frequency-by-frequency correlation (off-diagonal, via coherence and phase). In simple terms, it tells the simulation how to make different signals move in a coordinated way rather than independently. It is essential for spatially distributed loading: without cross-spectra, the numerical procedure would apply uncorrelated forces along the tower and misrepresent total base shear. The multivariate spectral representation method is due to [38, 115], with the random-vibration background in [92, 103]. A useful mental model is that the cross-spectral matrix is the frequency-domain analogue of the covariance matrix, and its Cholesky factorization is exactly what the simulation uses to generate correlated series [115]. The paper's wind-and-wave records are therefore not independent inputs but one coherent multivariate realization.

For an n-component process $\boldsymbol{X}(t)$, the spectral density matrix $\mathbf{S}_{XX}(\omega)$ is Hermitian (equal to its own conjugate transpose) and positive semidefinite. Its entries satisfy

$$S_{ij}(\omega) = \gamma_{ij}(\omega)\sqrt{S_{ii}(\omega)S_{jj}(\omega)}, \qquad |\gamma_{ij}(\omega)| \leq 1. \tag{8}$$

A valid synthesis requires all eigenvalues of $\mathbf{S}_{XX}$ to be nonnegative. Cholesky or eigenfactorization transforms independent complex Gaussian ordinates into correlated components.

In the reference paper, the cross-spectral matrix is the device that turns the separate wind and wave descriptions into a single coherent multivariate realization: the wind histories over the rotor blades and tower height and the wave kinematics acting along the tower are generated jointly rather than independently, so that total base shear and base moment reflect their correlation. In the computational program the same matrix is used in the multivariate spectral-representation synthesis, where its Cholesky (or eigen-) factorization converts independent complex Gaussian ordinates into the correlated wind-and-wave series that drive the time-domain simulation [38, 115].

3 Linear Wave Theory in Finite Depth

3.1 Linear potential-flow assumptions

Linear (Airy) wave theory describes small-amplitude waves as the superposition of sinusoidal components satisfying Laplace's equation with linearized free-surface conditions. Its power lies in linearity: any irregular sea becomes a sum of independent regular waves, each obeying the dispersion relation. This is the baseline against which all nonlinear corrections are measured, and the regime in which the numerical procedure is exact. The theory originates with [52, 119], is developed rigorously in [87, 89, 128], and is presented for engineers in [10, 94]; the offshore perspective is given in [16, 104]. The celebrated consequence is the dispersion relation $\omega^2 = gk\tanh kh$, which ties every

frequency to a wavelength and thus to the spatial scale of loading. Because the relation is exact within the linear approximation, the numerical verification procedure can test the numerical procedure against it with machine precision [10].

The fluid is taken as incompressible, inviscid, and irrotational away from boundary layers. The velocity potential satisfies

$$\nabla^2 \Phi = 0, \tag{9}$$

with impermeable-bed condition $\partial\Phi/\partial z = 0$ at $z = -h$. At the free surface $z = \eta(x,t)$ the kinematic condition

$$\frac{\partial \eta}{\partial t} + \frac{\partial \Phi}{\partial x}\frac{\partial \eta}{\partial x} = \frac{\partial \Phi}{\partial z} \tag{10}$$

states that a fluid particle on the surface remains on the surface, and the dynamic condition

$$\frac{\partial \Phi}{\partial t} + \frac{1}{2}\left[\left(\frac{\partial \Phi}{\partial x}\right)^2 + \left(\frac{\partial \Phi}{\partial z}\right)^2\right] + g\eta = 0 \tag{11}$$

states that the pressure at the free surface is atmospheric. Both conditions are imposed at the unknown position $z = \eta$. Linearization of the free-surface conditions about $z = 0$ gives

$$\frac{\partial \eta}{\partial t} = \frac{\partial \Phi}{\partial z}, \qquad \frac{\partial \Phi}{\partial t} + g\eta = 0. \tag{12}$$

A harmonic solution yields the dispersion relation

$$\omega^2 = gk \tanh(kh). \tag{13}$$

The relation is monotone in $k > 0$ and may be solved by Newton iteration,

$$k_{r+1} = k_r - \frac{gk_r \tanh(k_r h) - \omega^2}{g \tanh(k_r h) + gk_r h \operatorname{sech}^2(k_r h)}. \tag{14}$$

3.2 Phase and group velocities

The phase velocity $c = \omega/k$ tracks individual crests, while the group velocity $c_g = d\omega/dk$ tracks the energy packet—and energy, not crests, is what loads the structure. In deep water $c_g = c/2$; in shallow water they coincide. The distinction matters because resonance of the tower depends on energy arriving at its natural frequencies, and because the numerical procedure must resolve the frequencies that carry energy, not merely those present in the record. Classical discussions appear in [89, 109, 128], with the engineering formulation in [10]. A striking implication is that in deep water individual crests travel twice as fast as the energy packet, so a tower feels energy arriving after the visible crests have passed. For design, what matters is that c_g sets the energy flux $\rho g a^2 c_g/2$ toward the structure [109].

The phase velocity and group velocity are

$$c = \frac{\omega}{k}, \qquad c_g = \frac{\partial \omega}{\partial k} = \frac{c}{2}\left(1 + \frac{2kh}{\sinh(2kh)}\right). \tag{15}$$

The deep-water limits are $c = g/\omega$ and $c_g = c/2$; the shallow-water limit is $c = c_g = \sqrt{gh}$. These limits are useful verification cases for the numerical dispersion solver.

3.3 Linear kinematics

Linear kinematics gives the water-particle velocity and acceleration beneath each wave component as explicit functions of depth, decaying as $\cosh k(z+h)/\cosh kh$. Simply put, it converts the surface elevation spectrum into the subsurface flow field that actually pushes on the tower members. This step is indispensable: the Morison equation needs velocities and accelerations at every submerged node, and the numerical procedure obtains them by superposing these analytical profiles. The expressions are derived in [10, 94]; their use in force computation follows [28, 114]. Note the exponential (deep water) or hyperbolic (finite depth) decay with depth: near the surface the orbital velocities are largest, which is why the upper tower segments dominate the drag load. The numerical procedure evaluates these profiles at each node depth, so vertical discretization directly controls load accuracy [114].

For component amplitude a, phase $\psi = \omega t - kx + \phi$, and $-h \le z \le 0$,

$$\eta = a\cos\psi, \tag{16}$$

$$u = a\omega\frac{\cosh k(z+h)}{\sinh kh}\cos\psi, \tag{17}$$

$$w = a\omega\frac{\sinh k(z+h)}{\sinh kh}\sin\psi, \tag{18}$$

$$\dot{u} = -a\omega^2\frac{\cosh k(z+h)}{\sinh kh}\sin\psi. \tag{19}$$

The transfer function grows toward the free surface and decays with depth. For high kh, direct evaluation of hyperbolic functions may overflow; scaled exponentials or asymptotic forms should be used.

3.4 Dynamic pressure and energy

Integrating the linearized Bernoulli equation yields the dynamic pressure field, and integrating pressure and kinetic energy over depth gives the energy density $E = \rho g a^2/2$ per component. Conceptually, this closes the energy budget: the spectrum prescribes energy input, and the pressure field is the mechanism delivering it to the structure. The numerical procedure uses dynamic pressure both to check energy conservation in verification tests and to compute distributed loads consistently with the velocity field. The foundations are in [87, 89], with the energy-flux viewpoint emphasized in [91, 109]. The dynamic pressure is also what a pressure transducer would measure, providing a direct experimental check of the theory; field validation of linear pressure transfer functions underpins their routine use [10]. In the paper, pressure-derived loads and velocity-derived loads must agree, giving an internal consistency test.

The linear dynamic pressure is

$$p'(x,z,t) = -\rho\frac{\partial\Phi}{\partial t} = \rho g a\frac{\cosh k(z+h)}{\cosh kh}\cos\psi. \tag{20}$$

The average energy per unit horizontal area is $E = \rho g H^2/8$ for a regular wave of height $H = 2a$. For an irregular sea, $E = \rho g m_0$ and $H_s \approx 4\sqrt{m_0}$ under the Gaussian narrow-band approximation.

4 Parametric Sea-State Spectra and Directionality

4.1 Pierson–Moskowitz spectrum

The Pierson–Moskowitz spectrum is the canonical model of a fully developed sea: it assumes the wind has blown long enough and over a long enough fetch that the sea state depends only on wind speed. Its ω^{-5} tail encodes Phillips' equilibrium-range physics, and its single peak reflects a mature sea. It is used here as the reference input spectrum because it is the simplest defensible choice for open-ocean conditions and the limiting case of fetch-limited models. The original derivation is [36]; the equilibrium-range argument is [108]; modern assessments appear in [4, 85], and the wave-forecasting context in [125]. The spectrum's single parameter—wind speed—is both its strength and its weakness: it cannot represent mixed wind-sea and swell systems, for which multi-peaked models such as Ochi–Hubble are needed [135]. The paper's choice of PM is therefore a deliberate simplification for a fully developed reference sea, stated explicitly as a benchmark condition.

A convenient frequency-domain form is

$$S_{PM}(\omega) = \alpha g^2\omega^{-5}\exp\left[-\beta\left(\frac{g}{U\omega}\right)^4\right]. \tag{21}$$

The classical fully developed values are $\alpha = 0.0081$ and $\beta = 0.74$.

An equivalent H_s-T_p parameterization is

$$S_{PM}(\omega) = \frac{5}{16}H_s^2\omega_p^4\omega^{-5}\exp\left[-\frac{5}{4}\left(\frac{\omega_p}{\omega}\right)^4\right]. \tag{22}$$

The discretized spectrum must be renormalized if the integration interval excludes a material fraction of m_0.

4.2 JONSWAP spectrum

The JONSWAP spectrum generalizes Pierson–Moskowitz to fetch-limited, growing seas by adding the peak-enhancement factor γ, producing the sharper spectral peak observed in the Joint North Sea Wave Project. Physically, it represents seas still receiving energy from the wind, with nonlinear transfer shaping the peak. It is needed whenever the design sea state is not fully developed—the usual case in coastal and fetch-limited sites. The experimental basis is [19]; the nonlinear-transfer physics behind the peak shape is [82]; applications and parameterizations are reviewed in [17, 23, 130]. The peak-enhancement factor γ (typically 1–7, mean 3.3) concentrates energy near ω_p, which sharpens resonant response of the tower's first mode; the paper's sensitivity study varies spectral shape precisely because extremes depend on it [19, 23].

The fetch-limited form introduces peak enhancement,

$$S_J(\omega) = A_\gamma S_{PM}(\omega)\gamma^{r(\omega)}, \tag{23}$$

$$r(\omega) = \exp\left[-\frac{(\omega-\omega_p)^2}{2\sigma^2\omega_p^2}\right], \tag{24}$$

$$\sigma = \begin{cases} 0.07, & \omega \le \omega_p, \\ 0.09, & \omega > \omega_p. \end{cases} \tag{25}$$

The factor A_γ enforces the target variance. Omitting it changes H_s when γ is varied.

4.3 Finite-depth and directional descriptions

Real seas are neither unidirectional nor in infinite depth: finite depth modifies the dispersion relation and shoals the waves, while directional spreading distributes energy over headings. The directional spectrum $S(\omega, \theta)$ captures both effects and is essential because a tower responds differently to beam versus head seas, and Morison loads depend on the normal velocity component. Ignoring directionality overestimates the coherence of loading along the structure. Directional modeling is treated in [14, 68, 99], with the finite-depth wave theory in [10, 94] and the engineering synthesis in [23]. A practical rule is that directionality reduces the effective excitation of modes whose shapes are orthogonal to the mean heading, while finite depth increases wavelengths and hence the correlation of loads over the water column. Both effects are first-order for shallow-water towers like the benchmark [10].

A directional spectrum is written

$$S_\eta(\omega, \theta) = S_\eta(\omega)D(\theta \mid \omega), \qquad \int_{-\pi}^{\pi} D(\theta \mid \omega)\mathrm{d}\theta = 1. \tag{26}$$

A cosine-power model has

$$D(\theta) = C_s \cos^{2s}\left(\frac{\theta-\theta_0}{2}\right), \tag{27}$$

where C_s is obtained from a beta-function normalization. Directionality modifies spatial coherence and force correlation, even when the point spectrum remains unchanged.

4.4 Spectral calibration

Spectral calibration adjusts a parametric spectrum so that its integrated moments reproduce target values of H_s and T_p (and the peak shape, if prescribed). In other words, it guarantees that the mathematical input to the numerical procedure actually represents the specified sea state—a mismatch here propagates into every response statistic. This step is required for reproducibility: two analysts given the same (H_s, T_p) must generate the same input energy. Calibration practice is discussed in [17, 34], and

the sensitivity of extremes to spectral shape is documented in [20, 73]. Calibration is typically done by scaling the spectrum so that $4\sqrt{m_0}$ equals the target H_s; the paper documents this renormalization because omitting it is a classic source of inter-model scatter in benchmark studies [17].

Given measured ordinates $\widehat{S}_i$, parameters $\boldsymbol{\theta}$ may be estimated by weighted least squares,

$$\widehat{\boldsymbol{\theta}} = \arg\min_{\boldsymbol{\theta}} \sum_i w_i [\log \widehat{S}_i - \log S(\omega_i; \boldsymbol{\theta})]^2, \tag{28}$$

or by a Whittle likelihood. Diagnostic plots should compare spectral area, peak frequency, bandwidth, and high-frequency moments rather than only visual agreement.

5 Spectral Representation and Time-Series Synthesis

5.1 Discrete random-phase representation

The random-phase model writes the sea surface as a sum of harmonic components with deterministic amplitudes from the spectrum and independent uniform random phases. Its justification is the central limit theorem: with many components, the surface becomes Gaussian regardless of the phase distribution. This is the conceptual engine of the entire time-domain simulation—each realization of the numerical procedure is one draw of the phase vector. The method and its statistical basis are presented in [38, 116, 122], with the oceanographic lineage in [26, 34]. An important subtlety is that the phases must be redrawn for every realization while amplitudes stay fixed: this is what makes records statistically independent yet identically distributed, the premise of all ensemble statistics in the paper [38].

For N_ω bands of width $\Delta\omega$,

$$\eta(t) = \sum_{j=1}^{N_\omega} a_j \cos(\omega_j t + \phi_j), \qquad a_j = \sqrt{2 S_\eta(\omega_j) \Delta\omega}, \quad \phi_j \sim U(0, 2\pi). \tag{29}$$

Jittering ω_j within each band can reduce artificial periodicity but removes strict compatibility with a standard equispaced FFT grid. In that case, complex recurrence evaluates the same harmonic sum efficiently over time:

$$z_j(t_{n+1}) = z_j(t_n) e^{\mathrm{i}\omega_j \Delta t}, \qquad \eta(t_n) = \Re \sum_j z_j(t_n). \tag{30}$$

This is a direct spectral representation, not a true IFFT, and its operation count is $\mathcal{O}(N_\omega N_t)$.

5.2 True IFFT representation

The inverse FFT turns the spectral representation into an algorithm: one FFT maps the complex spectral amplitudes to a full time series in $O(N \log N)$ operations. Mathematically it is identical to the direct summation, but it makes 3-hour simulations with tens of thousands of steps computationally feasible. It is the reason the numerical

procedure can afford long records and hence stable extreme statistics. The FFT algorithm is [62]; its application to random-process simulation is [38]; practical guidance appears in [57, 103]. The IFFT imposes periodicity on the generated record, so the paper discards transient-affected edges or uses circular embedding; the "true" qualifier in the subsection title refers to enforcing exact spectral amplitudes rather than randomized ones [38].

For a uniform grid $\omega_k = k\Delta\omega$ with $\Delta\omega = 2\pi/T$, Hermitian coefficients satisfy $X_{N-k} = X_k^*$ and

$$x_n = \frac{1}{N} \sum_{k=0}^{N-1} X_k e^{\mathrm{i}2\pi kn/N}. \tag{31}$$

The scaling of X_k depends on the FFT convention. Verification is performed by Parseval closure,

$$\sum_{n=0}^{N-1} |x_n|^2 = \frac{1}{N} \sum_{k=0}^{N-1} |X_k|^2. \tag{32}$$

5.3 Sampling and aliasing

Sampling replaces the continuous spectrum by a periodic one: energy above the Nyquist frequency folds back and contaminates the resolved band. Simply stated, a too-large time step invents spurious low-frequency energy and corrupts both fatigue and extreme estimates. The numerical procedure must therefore choose Δt (and the spectral cutoff) so that the energy-containing and structurally relevant frequencies lie well below Nyquist. The sampling theorem and its consequences are classical [57, 110]; the structural-dynamics viewpoint, linking Δt to the highest retained modal frequency, is stressed in [5, 8]. A useful check the paper applies is energy conservation: the variance of the generated series must match m_0 of the target spectrum to within tolerance, otherwise aliasing or truncation has corrupted the input [57].

The Nyquist frequency is $\omega_N = \pi/\Delta t$. The upper environmental cutoff, quadratic sum frequencies, and retained structural modes must remain below ω_N. A conservative accuracy condition is

$$\Delta t\, \omega_{\max} \leq 0.2 \text{ to } 0.3, \tag{33}$$

which is an accuracy criterion rather than a universal stability theorem. Record duration controls the lowest resolvable frequency and the uncertainty of extremes.

5.4 Statistical convergence

A single 3-hour realization is one sample of a random experiment; its block maximum is itself random. Statistical convergence analysis asks how many records (or how long a record) are needed for stable estimates of means, variances, and extremes. This is indispensable because the numerical procedure's headline results—return values of base shear and moment—are only as credible as their sampling variability. Convergence of spectral estimates is treated in [57, 110], and the specific problem of stable

extreme estimates from limited records in [46, 102]. The paper's choice of twenty 3-hour records reflects this trade-off: long enough for stable second moments, marginal for tail quantiles—which is exactly why L-moments and POT are brought in later [46].

For R independent realizations, the ensemble estimate of a statistic g is

$$\overline{g}_R = \frac{1}{R}\sum_{r=1}^{R} g_r, \qquad \mathrm{SE}(\overline{g}_R) = \frac{s_g}{\sqrt{R}}. \tag{34}$$

Convergence should be reported for variance, skewness, kurtosis, crossing rates, peak correlation, and response maxima. Reusing the same phases across model alternatives is recommended for variance reduction in comparative studies.

6 Second-Order Irregular Waves and Quadratic Interactions

6.1 Perturbation expansion

The Stokes perturbation expands velocity potential and surface elevation in powers of the wave steepness $\epsilon = ka$, solving Laplace's equation order by order. At first order it recovers Airy theory; at second order it produces bound harmonics—sharper crests, flatter troughs—without new free waves. Conceptually, it is the systematic way to add finite-amplitude physics while keeping the linear spectral machinery. The numerical procedure uses it to generate the nonlinear free surface whose kinematics drive the loads. The expansion originates with [119]; its modern exposition is [71, 94]; finite-depth second-order theory is [64]. The ordering parameter is the steepness $\epsilon = ka$, and the theory assumes $\epsilon \ll 1$; the paper's $H_s = 5.5\,\mathrm{m}$, $T_p = 13\,\mathrm{s}$ sea gives moderate steepness, inside the working range but close enough to motivate the validity discussion [71].

Under weak nonlinearity, free-surface elevation and potential are expanded as

$$\eta = \varepsilon\eta^{(1)} + \varepsilon^2\eta^{(2)} + \mathcal{O}(\varepsilon^3), \qquad \Phi = \varepsilon\Phi^{(1)} + \varepsilon^2\Phi^{(2)} + \mathcal{O}(\varepsilon^3). \tag{35}$$

Second-order terms contain sum-frequency and difference-frequency interactions. Difference terms may excite slow drift and flexible structural modes, whereas sum terms sharpen crests and flatten troughs.

6.2 Quadratic transfer functions

Quadratic transfer functions (QTFs) encode, for each pair of first-order components, the amplitude and phase of the resulting sum- and difference-frequency second-order wave. They are the complete algebraic summary of second-order wave–wave interaction: once known, the nonlinear surface is a double sum over component pairs. In the numerical procedure they are the bridge between the input spectrum and the nonlinear kinematics—and the reason second-order simulations are far costlier than linear ones. The directional QTF theory is [45]; the underlying interaction physics is [82, 90]; engineering implementation is discussed in [2]. Sum-frequency QTFs drive high-frequency "ringing"-type loads while difference-frequency QTFs drive slow drift;

the paper retains both because the tower's first mode can be excited by difference frequencies of energetic wave groups [45].

For complex first-order amplitudes A_m,

$$\eta_+^{(2)}(t) = \Re \sum_{m=1}^{N} \sum_{n=1}^{N} Q_{mn}^{+} A_m A_n e^{\mathrm{i}(\omega_m + \omega_n)t}, \tag{36}$$

$$\eta_-^{(2)}(t) = \Re \sum_{m=1}^{N} \sum_{n=1}^{N} Q_{mn}^{-} A_m A_n^{*} e^{\mathrm{i}(\omega_m - \omega_n)t}. \tag{37}$$

Symmetry requires $Q_{mn}^{+} = Q_{nm}^{+}$ and an appropriate conjugate symmetry for the difference kernel. Diagonal terms, zero differences, and double counting need explicit conventions.

6.3 Direct and condensed summation

The double sum over component pairs scales as $O(N^2)$ and dominates the cost of second-order synthesis. Direct summation evaluates every pair; condensed (or efficient) summation exploits symmetries and frequency-domain structure to reduce the burden. This is not a modeling choice but a computational one: it determines whether 3-hour second-order records are affordable at all, and therefore whether the nonlinear statistics in this paper can be estimated. Efficient second-order simulation is addressed in [3]; the interaction-count problem is analyzed in [82]; and the trade-off between fidelity and cost frames the modernization discussion in the numerical procedure. The $O(N^2)$ bottleneck is the reason many industrial codes still run linear seas: the paper accepts the cost deliberately, because the linear/nonlinear comparison is its scientific point [3].

Direct evaluation requires $\mathcal{O}(N^2 N_t)$ operations. When frequencies occupy uniform bins, pairs with equal sum or difference index can be condensed:

$$B_p^{+} = \sum_{m+n=p} Q_{mn}^{+} A_m A_n, \qquad B_q^{-} = \sum_{m-n=q} Q_{mn}^{-} A_m A_n^{*}. \tag{38}$$

The time series then becomes a one-dimensional harmonic sum. The condensed and direct forms must be compared using identical phases and kernels.

6.4 Second-order kinematics

Second-order kinematics adds the bound-wave velocity and acceleration fields to their linear counterparts, producing the asymmetric orbital motion—stronger forward velocities under crests—characteristic of steep seas. Since Morison drag scales with velocity squared, this asymmetry directly amplifies extreme loads beyond linear predictions. The numerical procedure therefore evaluates second-order kinematics at every submerged node before forming the loads. The theory is given in [45, 64]; its effect on crest statistics in [74, 120]; and on structural response in [50, 101]. The bound harmonics travel locked to the primary wave groups rather than obeying the linear dispersion

relation—a frequent source of confusion the paper avoids by computing kinematics directly from the QTF synthesis [64].

Velocity and acceleration follow by time and spatial differentiation of the second-order potential. If a component is represented by $Be^{i\Omega t}$, differentiation gives

$$\frac{\mathrm{d}}{\mathrm{d}t}(Be^{i\Omega t}) = i\Omega Be^{i\Omega t}, \qquad \frac{\mathrm{d}^2}{\mathrm{d}t^2}(Be^{i\Omega t}) = -\Omega^2 Be^{i\Omega t}. \tag{39}$$

Sign and phase conventions must remain consistent between elevation, velocity, and acceleration. A single-component Stokes-wave test is the preferred analytical check.

6.5 Validity limits

Stokes theory is asymptotic: it converges only for moderate steepness and fails near breaking (Miche's criterion) and in very shallow water (Ursell number large), where higher-order or fully nonlinear theories are required. These limits define the domain of credibility of the entire numerical procedure—results computed outside it are not conservative, they are meaningless. Stating them is therefore a scientific obligation, not a formality. The classical limits are [98, 123]; breaking physics is reviewed in [53, 97]; and the transition to strongly nonlinear regimes (freak waves) in [58, 100, 106, 131]. The Ursell number $U_r = HL^2/h^3$ is the practical gauge: for the benchmark ($h = 20\,\mathrm{m}$) it stays in the Stokes regime, but the paper flags that shallower sites would require cnoidal or stream-function theory [71, 134].

Weakly nonlinear models require moderate steepness and absence of breaking. Indicators include ka, H/h, Ursell number $Ur = HL^2/h^3$, and proximity to breaking criteria. Extrapolation of subsurface kinematics into the instantaneous crest region should be disclosed and tested against Wheeler stretching or higher-order alternatives.

7 Wind Field, Harris Turbulence, and Aerodynamic Loading

7.1 Mean wind profiles

The mean wind profile (logarithmic or power law) describes how the 10-minute mean wind speed grows with height above the sea. It sets the steady aerodynamic thrust on the rotor and tower—the static preload about which turbulence-induced dynamics oscillate. In the numerical procedure it fixes the operating point of the aerodynamic load model. The logarithmic law and its offshore roughness treatment are classical [65, 117]; the power-law alternative and its calibration are discussed in [48, 69]. Offshore, the roughness length is an order of magnitude smaller than on land, so the profile is fuller and hub-height winds stronger for the same 10-m reference—a fact the paper's z_0 choice encodes [117].

Two common profiles are

$$\overline{U}(z) = U_r \left(\frac{z}{z_r}\right)^{\alpha}, \qquad \overline{U}(z) = \frac{u_*}{\kappa} \ln\left(\frac{z-d}{z_0}\right). \tag{40}$$

The power-law exponent and roughness length depend on stability, surface condition, and averaging duration. They should be calibrated rather than treated as universal constants.

7.2 Harris-type turbulence spectrum

The Harris spectrum distributes turbulent kinetic energy over frequency, with a peak at the large-eddy scale and a $-5/3$ inertial subrange. In plain terms, it tells the simulation which gust frequencies shake the tower most—typically near its first natural frequency, where resonant amplification occurs. It is needed because quasi-steady gusts at the wrong frequencies would misrepresent the dynamic amplification of the response. The spectrum is [18, 81]; the broader family of wind spectra (Kaimal, Davenport) is [25, 65]; offshore application is [105]. The Harris spectrum's length scale grows with height, so the tower top sees larger, slower eddies than the base; the numerical procedure accounts for this height dependence in the synthesis [81].

A general Harris form may be represented as

$$S_u(f) = \frac{4C_m U L}{[2 + (fL/U)^2]^{5/6}}, \tag{41}$$

subject to the exact frequency convention used for f or ω. Dimensional analysis requires S_u to have units of velocity squared per frequency. The integral must recover the target variance. Dimensional consistency gives $C_m = (\sigma_u/\overline{U})^2$, the squared turbulence intensity.

7.3 Coherence and correlated synthesis

Coherence quantifies how similar the turbulence is at two separated points as a function of frequency; the numerical procedure uses it to synthesize correlated wind histories over the rotor blades and tower height. Without it, gusts would strike all points independently, destroying the spatial correlation that governs total thrust fluctuations. This step converts single-point spectra into a physically consistent wind field. Coherence models originate with [65]; correlated simulation methods are [115, 118]; and the structural-loading implications are developed in [69, 117]. The Davenport exponential coherence decay with separation and frequency is the default model, and the paper adopts it for lack of site-specific measurements—a documented assumption, not a validated fact [65].

For elevations z_i and z_j,

$$\gamma_{ij}(f) = \exp\left[-C_c \frac{f|z_i - z_j|}{\overline{U}}\right], \tag{42}$$

and the cross-spectrum is

$$S_{ij}(f) = \gamma_{ij}(f)\sqrt{S_i(f)S_j(f)}e^{-\mathrm{i}2\pi f \tau_{ij}}. \tag{43}$$

At each frequency, factorization $\mathbf{S} = \mathbf{L}\mathbf{L}^H$ gives $\widehat{\boldsymbol{u}} = \mathbf{L}\boldsymbol{\xi}$, with independent complex Gaussian $\boldsymbol{\xi}$.

7.4 Aerodynamic force

The aerodynamic force combines the mean thrust from the wind profile with fluctuating components from turbulence, typically via a quasi-steady blade-element or thrust-coefficient model. It closes the environmental input side: waves load the submerged part, wind loads the exposed part, and their joint action drives the tower dynamics. In the numerical procedure it must be synchronized with the wave record so that combined extremes are captured. Aerodynamic loading of structures is treated in [69, 117], with the offshore wind-turbine context in [48]. Because aerodynamic damping from the rotor can rival structural damping, the paper's combined wind–wave simulations capture an effect that wave-only benchmarks miss entirely [48].

A quasi-steady drag model is

$$F_a(t) = \frac{1}{2}\rho_a C_S A_p |U(t) - \dot{x}_s(t)|[U(t) - \dot{x}_s(t)]. \tag{44}$$

Linearization about mean speed $\overline{U}$ yields an aerodynamic damping contribution proportional to $\rho_a C_S A_p \overline{U}$. The full quadratic form should be retained when response non-Gaussianity is of interest.

8 Morison-Type Hydrodynamic Loading

8.1 Fixed and moving-member forms

The Morison equation decomposes the wave force on a slender cylinder into an inertia term (proportional to fluid acceleration) and a drag term (proportional to velocity squared), with the relative-motion form accounting for structural velocity. It is the constitutive law of offshore hydrodynamics for small-diameter members: it turns the kinematic fields into nodal forces. Every load in the numerical procedure passes through it, so its coefficients and form control the entire force level. The original formulation is [28]; the relative-motion extension and coefficient systematics are [113, 114]; the offshore design context is [1, 13]. The equation is semi-empirical: C_D and C_M must come from experiments at matching KC and Re, and the paper's use of constant coefficients is flagged as a leading uncertainty [114].

For a circular member of diameter D and displaced area $A_D = \pi D^2/4$,

$$q(t) = \frac{1}{2}\rho C_D D |U_r| U_r + \rho C_M A_D \dot{u} - \rho(C_M - 1) A_D \ddot{x}_s, \tag{45}$$

where $U_r = u + U_c - \dot{x}_s$. Alternative conventions combine the structural-acceleration term with the left-hand-side mass matrix. The chosen convention must avoid double counting added mass.

8.2 Dimensionless parameters

The Keulegan–Carpenter number KC, Reynolds number Re, and diffraction parameter D/L classify the flow regime: they decide whether inertia or drag dominates, whether vortex shedding matters, and whether Morison's slender-body assumption holds at all. In short, they are the diagnostic that licenses the use of the Morison

equation for this tower ($D/L \ll 1$, moderate KC). The numerical procedure checks them before trusting any load. The regime map originates with [84]; the vortex-shedding and roughness effects with [112]; and the synthesis for designers with [7, 39]. For the benchmark, $KC \approx 11$ places the flow in the drag–inertia transition where both terms matter—neither can be dropped, which is why the paper keeps the full Morison form [84].

The influential groups are

$$KC = \frac{U_m T}{D}, \qquad Re = \frac{U_m D}{\nu}, \qquad \beta = \frac{Re}{KC} = \frac{D^2}{\nu T}. \tag{46}$$

The coefficients C_D and C_M depend on roughness, KC, Reynolds number, proximity to boundaries, free-surface effects, and wave-current interaction. Constant coefficients are an engineering approximation and a major source of uncertainty.

8.3 Statistical structure of quadratic drag

Because drag is quadratic in velocity, a Gaussian velocity field produces a non-Gaussian (chi-square-like) force with non-zero mean—the well-known drift component—and skewed extremes. This is the first and strongest source of non-Gaussianity in the response chain, preceding any structural nonlinearity. Understanding it is essential because it explains why linear spectral analysis systematically misestimates drag-dominated extremes. The statistics of quadratic transformations of Gaussian processes are developed in [78, 102]; the ocean-wave application in [101, 120]. The non-zero mean of the drag force is the steady drift load that preloads the tower; the paper's static offset analysis separates it from the dynamic part before extreme-value fitting [78].

If $U \sim N(0, \sigma_U^2)$, the mean of $|U|U$ is zero and

$$\mathbb{E}[(|U|U)^2] = \mathbb{E}[U^4] = 3\sigma_U^4. \tag{47}$$

With nonzero mean current, odd moments no longer vanish. For $U_r = \mu_U + \sigma_U Z$, the expected drag can be obtained from truncated-normal moments or numerical quadrature. This illustrates why current changes both mean load and fluctuation intensity.

8.4 Wetting and load integration

Wetting refers to evaluating kinematics up to the instantaneous free surface rather than the mean water level; load integration then sums member forces into total base shear and overturning moment. Physically, the crest zone—where velocities are largest—contributes disproportionately, so truncating at mean sea level underestimates extremes. The numerical procedure therefore stretches or extrapolates kinematics into the crest (e.g., Wheeler stretching) before integrating. The stretching method is [127]; the importance of the crest zone for forces is shown in [74]; and the integration practice follows [13, 114]. Wheeler stretching maps the $z = 0$ kinematics to the instantaneous surface by a simple coordinate transform; it is approximate but standard, and the paper notes it as a modeling choice with known bias [127].

The instantaneous wetted interval terminates at $z = \eta(t)$. The consistent element load is

$$\boldsymbol{f}_e(t) = \int_{L_e \cap \Omega_w(t)} \mathbf{N}^T(s) q(s,t) \mathrm{d}s. \tag{48}$$

Discontinuous wetting can inject high-frequency content. Smoothing the wetting function may improve numerical behavior but changes the physical model and must be studied by refinement.

8.5 Linearization for response estimates

Equivalent linearization replaces the quadratic drag with a linear damping-like term matched in mean square, enabling closed-form spectral response analysis. It is a pragmatic shortcut: it preserves the energy dissipation of drag while restoring the linear machinery of transfer functions. In the numerical procedure it serves as the fast reference solution against which fully nonlinear time-domain results are compared—the linear/nonlinear ratios reported later. The method's theory is [63]; its offshore application is [114]; and its limitations for extremes motivate the nonlinear simulations [102]. The equivalent linear damping depends on the response level itself, so the paper iterates the linearization—a detail that distinguishes a careful implementation from a one-shot approximation [63].

Equivalent linearization replaces drag by $c_h U_r$ with

$$c_h = \frac{\mathbb{E}[q_D U_r]}{\mathbb{E}[U_r^2]}. \tag{49}$$

For zero-mean Gaussian velocity,

$$c_h = \frac{1}{2}\rho C_D D \frac{\mathbb{E}[|U|U^2]}{\sigma_U^2} = \rho C_D D \sigma_U \sqrt{\frac{2}{\pi}}. \tag{50}$$

The approximation is useful for FRF studies but cannot reproduce non-Gaussian tails.

9 Finite-Element Formulation for Slender Structures

9.1 Planar frame element

The planar frame (beam-column) element discretizes the tower into segments carrying axial, shear, and bending action, with cubic transverse shape functions. It is the mechanical atom of the model: assembling elements reproduces the continuous tower's stiffness with controllable accuracy. The numerical procedure needs it because closed-form solutions do not exist for tapered, mass-loaded towers. The element formulation is standard [5, 83, 132], with the structural-dynamics context in [8, 61]. Cubic Hermite shape functions give exact nodal solutions for prismatic beams under point loads, which is why a modest element count already converges the tower's first modes [5].

For local degrees of freedom $[u_1, v_1, \theta_1, u_2, v_2, \theta_2]^T$, the Euler–Bernoulli stiffness matrix combines axial and bending terms. The bending block is

$$\mathbf{K}_b = \frac{EI}{L^3}\begin{bmatrix} 12 & 6L & -12 & 6L \\ 6L & 4L^2 & -6L & 2L^2 \\ -12 & -6L & 12 & -6L \\ 6L & 2L^2 & -6L & 4L^2 \end{bmatrix}. \tag{51}$$

The axial block has EA/L multiplying $\begin{bmatrix} 1 & -1 \\ -1 & 1 \end{bmatrix}$. Transformation to global axes uses $\mathbf{K}_e^g = \mathbf{T}^T \mathbf{K}_e^l \mathbf{T}$.

9.2 Consistent mass

The consistent mass matrix derives from the same shape functions as the stiffness matrix, distributing each element's inertia according to the assumed deformation pattern rather than lumping it at nodes. This matters because the tower's natural frequencies—the quantities that decide resonance with wave and wind spectra—are eigenvalues of the mass–stiffness pair, and lumped mass can distort higher modes. The formulation and its convergence properties are given in [5, 83], with the vibration-theory background in [75, 95]. A useful diagnostic is that consistent mass overestimates frequencies while lumped mass underestimates them, bracketing the true values—the paper exploits this in verification [5].

The bending consistent-mass matrix is

$$\mathbf{M}_b = \frac{\rho_A L}{420}\begin{bmatrix} 156 & 22L & 54 & -13L \\ 22L & 4L^2 & 13L & -3L^2 \\ 54 & 13L & 156 & -22L \\ -13L & -3L^2 & -22L & 4L^2 \end{bmatrix}. \tag{52}$$

Consistent mass generally predicts modal properties more accurately than lumped mass for the same mesh. Added hydrodynamic mass may be assembled consistently or treated through the force model, but not both.

9.3 Truss and spring contributions

Truss elements (axial only) and discrete springs represent braces, appurtenances, and foundation flexibility within the same assembly. They allow the model to include secondary load paths and soil compliance without meshing them as frames. In the numerical procedure they are the mechanism for support conditions that shift the fundamental frequency—a first-order effect on dynamic amplification. The treatment of mixed element types is covered in [5, 83, 132]. Foundation springs are the paper's pragmatic stand-in for soil–structure interaction; their stiffness is varied in the sensitivity study because it moves the fundamental frequency across the wave-energy band [61].

A two-dimensional truss contributes only axial stiffness in local coordinates. A translational or rotational spring between paired degrees of freedom has

$$\mathbf{K}_s = k\begin{bmatrix} 1 & -1 \\ -1 & 1 \end{bmatrix}. \tag{53}$$

Springs may represent foundation compliance, braces, or localized connections. Their units and associated degrees of freedom must be explicit.

9.4 Global assembly and constraints

Assembly enforces displacement compatibility at shared nodes, building the global stiffness, mass, and damping matrices from element contributions; constraints then impose supports and rigid links. This is where the finite-element discretization becomes a single system of ordinary differential equations—the object actually integrated in time. Errors here (wrong connectivity, over-constraint) corrupt every downstream result, which is why the verification section tests assembly on known cases. The assembly procedure is [5, 83], with the equation-of-motion viewpoint in [8, 61]. The assembled system for the tower has only a few hundred degrees of freedom, small by modern standards, which is precisely what makes 3-hour nonlinear time-domain simulation affordable [5].

Using Boolean connectivity matrices $\mathbf{A}_e$,

$$\mathbf{K} = \sum_e \mathbf{A}_e^T \mathbf{K}_e \mathbf{A}_e, \qquad \mathbf{M} = \sum_e \mathbf{A}_e^T \mathbf{M}_e \mathbf{A}_e, \qquad \boldsymbol{f} = \sum_e \mathbf{A}_e^T \boldsymbol{f}_e. \tag{54}$$

Constraint elimination is preferred to artificial diagonal values in eigenanalysis. The assembled unconstrained matrices should be symmetric, and the constrained mass matrix should remain positive definite.

9.5 Internal forces and reactions

Recovering internal forces (axial, shear, bending moment) from nodal displacements via the element constitutive relations is the final mechanical step: design decisions are made on these quantities, not on displacements. Base shear and overturning moment—the extreme statistics reported later—are reactions obtained here. The numerical procedure must therefore recover forces with the same shape functions used for stiffness, or equilibrium is violated. Stress recovery is treated in [5, 132], and the design relevance of base reactions in [1, 13]. Because extremes of base moment—not displacement—govern overturning design, the paper's entire statistical machinery is aimed at these recovered quantities [1].

Element forces are recovered from

$$\boldsymbol{s}_e = \mathbf{K}_e^l \boldsymbol{u}_e^l - \boldsymbol{f}_{e,\mathrm{eq}}^l. \tag{55}$$

Support reactions follow from the complete equilibrium equation before restrained degrees are removed. Dynamic reactions include inertia and damping effects when those contributions act at the supports.

10 Modal Analysis, Damping, and Model Reduction

10.1 Generalized eigenproblem

The generalized eigenproblem $K\phi = \omega^2 M\phi$ extracts the tower's natural frequencies and mode shapes—the fingerprints of its dynamics. Physically, each mode is a pattern in which the structure "wants" to vibrate; the first few dominate the response to broadband wave loading. The numerical procedure needs them both for physical

insight and as the basis of modal reduction. The theory is [8, 75, 95]; numerical solution methods are [5, 55]. The eigenvectors are M-orthogonal, which is the algebraic property that makes modal decoupling possible in the first place [8].

Undamped free vibration satisfies

$$(\mathbf{K} - \omega_r^2 \mathbf{M})\boldsymbol{\phi}_r = \mathbf{0}. \tag{56}$$

For symmetric positive-definite $\mathbf{M}$ and semidefinite $\mathbf{K}$, real nonnegative eigenvalues are expected after appropriate constraints. Mass normalization gives

$$\boldsymbol{\phi}_r^T \mathbf{M} \boldsymbol{\phi}_s = \delta_{rs}, \qquad \boldsymbol{\phi}_r^T \mathbf{K} \boldsymbol{\phi}_s = \omega_r^2 \delta_{rs}. \tag{57}$$

10.2 Modal projection

Modal projection rewrites the coupled equations of motion in the basis of mode shapes, decoupling them into independent single-degree-of-freedom oscillators (for proportional damping). Conceptually, it replaces thousands of nodal unknowns by a handful of modal coordinates—the key to affordable long-duration simulation. The numerical procedure uses it to integrate 3-hour records that would be prohibitive in physical coordinates. The method is classical [8, 61, 75], with the computational implications in [5]. Truncation to the first few modes is justified because wave spectra carry little energy above $\sim$1 Hz while the tower's higher modes lie well above it—a physical, not merely numerical, argument [61].

With $\boldsymbol{x} \approx \boldsymbol{\Psi} \boldsymbol{q}$,

$$\mathbf{M}_m \ddot{\boldsymbol{q}} + \mathbf{C}_m \dot{\boldsymbol{q}} + \mathbf{K}_m \boldsymbol{q} = \boldsymbol{\Psi}^T \boldsymbol{f}(t), \tag{58}$$

where $\mathbf{M}_m = \boldsymbol{\Psi}^T \mathbf{M} \boldsymbol{\Psi}$. Classical damping makes $\mathbf{C}_m$ diagonal. Nonproportional damping requires coupled modal equations or a state-space eigensolution.

10.3 Participation and truncation

Modal participation factors measure how much each mode contributes to a given response quantity; truncation keeps only the significant modes. The subtlety is that displacement converges faster than internal forces—shear and moment need more modes—so the truncation criterion must be tied to the quantity of interest. In the numerical procedure, effective-mass closure plus direct convergence checks decide the retained set. Participation theory is [8, 61]; the force-versus-displacement convergence distinction is emphasized in [5, 75]. The paper reports cumulative effective mass above 90% as its truncation criterion, the threshold recommended in seismic and offshore practice [61].

For influence vector $\boldsymbol{r}$, the participation factor and effective mass are

$$\Gamma_j = \frac{\boldsymbol{\phi}_j^T \mathbf{M} \boldsymbol{r}}{\boldsymbol{\phi}_j^T \mathbf{M} \boldsymbol{\phi}_j}, \qquad M_j^* = \Gamma_j^2 \boldsymbol{\phi}_j^T \mathbf{M} \boldsymbol{\phi}_j. \tag{59}$$

A modal basis should be selected by cumulative effective mass and by direct convergence of the response quantity, especially local bending moments.

10.4 Rayleigh damping

Rayleigh damping builds the damping matrix as a linear combination of mass and stiffness, $C = \alpha M + \beta K$, calibrated to prescribed damping ratios at two frequencies. It is a mathematical convenience rather than a physical model, but it is the industry standard for representing the many unmodeled dissipation mechanisms. The numerical procedure uses it to set realistic resonant amplification; the caveat—spurious damping of higher modes—is why the calibration frequencies must bracket the excited band. The formulation is [8, 61]; critical discussion is [75]. Calibrating at the first two modal frequencies is standard, but the paper checks that the resulting damping at wave frequencies stays within physically plausible bounds [8].

For $\mathbf{C} = \alpha_M \mathbf{M} + \alpha_K \mathbf{K}$,

$$\zeta(\omega) = \frac{1}{2}\left(\frac{\alpha_M}{\omega} + \alpha_K \omega\right). \tag{60}$$

Specifying damping at two frequencies gives a two-equation system. Rayleigh damping may overdamp modes outside the calibration interval, so the resulting curve should always be plotted.

10.5 Eigenpair verification

Verifying computed eigenpairs against analytical benchmarks (uniform beam frequencies, orthogonality, mass closure) is the gate that certifies the structural model before any loading is applied. A wrong mode shape would silently corrupt every response statistic, so this check is non-negotiable in the verification hierarchy. The numerical procedure performs it as a unit test with tight tolerances. Reference solutions are [75, 95]; experimental counterpart practice (modal testing) is [70]. Even the sign and scaling of mode shapes are checked, because participation factors change sign with them—a classic source of silent error [70].

Each eigenpair is assessed by

$$r_j = \frac{\|\mathbf{K}\boldsymbol{\phi}_j - \omega_j^2 \mathbf{M}\boldsymbol{\phi}_j\|_2}{\|\mathbf{K}\boldsymbol{\phi}_j\|_2 + \omega_j^2 \|\mathbf{M}\boldsymbol{\phi}_j\|_2}. \tag{61}$$

Orthogonality matrices $\boldsymbol{\Psi}^T \mathbf{M} \boldsymbol{\Psi}$ and $\boldsymbol{\Psi}^T \mathbf{K} \boldsymbol{\Psi}$ reveal scaling and ordering errors.

11 Explicit Time Integration by Runge–Kutta

11.1 State-space representation

The state-space form recasts the second-order equations as a first-order system $\dot{y} = f(y, t)$, the standard input format for ordinary-differential-equation solvers. It is a change of language, not physics, but it unifies the treatment of structural dynamics, control, and explicit integration under one mathematical roof. The numerical procedure uses it to deploy Runge–Kutta schemes. The formulation is [61, 75], with the ODE-theory background in [59, 80]. Doubling the system size (displacements plus velocities) is the price of first-order form, gladly paid for access to the mature ODE solver literature [80].

The second-order system

$$\mathbf{M}\ddot{\boldsymbol{x}} + \mathbf{C}\dot{\boldsymbol{x}} + \mathbf{K}\boldsymbol{x} = \boldsymbol{f}(t) \tag{62}$$

becomes

$$\dot{\boldsymbol{y}} = \begin{bmatrix} \mathbf{0} & \mathbf{I} \\ -\mathbf{M}^{-1}\mathbf{K} & -\mathbf{M}^{-1}\mathbf{C} \end{bmatrix} \boldsymbol{y} + \begin{bmatrix} \mathbf{0} \\ \mathbf{M}^{-1} \end{bmatrix} \boldsymbol{f}(t), \quad \boldsymbol{y} = \begin{bmatrix} \boldsymbol{x} \\ \dot{\boldsymbol{x}} \end{bmatrix}. \tag{63}$$

Explicit formation of $\mathbf{M}^{-1}$ is unnecessary; linear solves are preferred.

11.2 Classical RK4

The classical fourth-order Runge–Kutta scheme advances the state with four stage evaluations per step, achieving fourth-order accuracy with an explicit (matrix-factorization-free) update. Its appeal is simplicity and high accuracy per step for smooth problems; its price is conditional stability, which caps the step size. In the numerical procedure it serves as the explicit reference solver for cross-checking the implicit results. The method and its order theory are [59, 80], with the engineering perspective in [5, 129]. The method's local error scales as Δt^5, so halving the step cuts the error by a factor of 32—the paper's temporal convergence study exploits exactly this scaling [59].

For $\dot{\boldsymbol{y}} = \boldsymbol{g}(t, \boldsymbol{y})$,

$$\boldsymbol{k}_1 = \boldsymbol{g}(t_n, \boldsymbol{y}_n), \tag{64}$$

$$\boldsymbol{k}_2 = \boldsymbol{g}(t_n + \tfrac{1}{2}\Delta t, \boldsymbol{y}_n + \tfrac{1}{2}\Delta t \boldsymbol{k}_1), \tag{65}$$

$$\boldsymbol{k}_3 = \boldsymbol{g}(t_n + \tfrac{1}{2}\Delta t, \boldsymbol{y}_n + \tfrac{1}{2}\Delta t \boldsymbol{k}_2), \tag{66}$$

$$\boldsymbol{k}_4 = \boldsymbol{g}(t_n + \Delta t, \boldsymbol{y}_n + \Delta t \boldsymbol{k}_3), \tag{67}$$

$$\boldsymbol{y}_{n+1} = \boldsymbol{y}_n + \frac{\Delta t}{6}(\boldsymbol{k}_1 + 2\boldsymbol{k}_2 + 2\boldsymbol{k}_3 + \boldsymbol{k}_4). \tag{68}$$

If the force depends on structural velocity, it should be recomputed at each RK stage for a fully coupled fourth-order treatment. Holding nonlinear force constant across the step reduces effective order.

11.3 Stability and accuracy

Stability asks whether numerical errors decay; accuracy asks how fast the error shrinks with Δt. For explicit schemes the two are linked through the stability limit $\omega_{\max}\Delta t \lesssim 2.8$—the step must resolve the fastest retained mode. This is the theoretical basis of the Nyquist caution noted in the results: violating it does not merely degrade accuracy, it can destabilize or alias the solution. Stability theory is [59, 80]; the structural-dynamics implications are [5, 8, 129]. The stability boundary is most restrictive for the highest retained mode, which is why modal truncation and time step cannot be chosen independently—a coupling the paper respects [5].

For $y' = \lambda y$, RK4 has amplification

$$R(z) = 1 + z + \frac{z^2}{2} + \frac{z^3}{6} + \frac{z^4}{24}, \qquad z = \lambda \Delta t. \tag{69}$$

Stability requires $|R(z)| \leq 1$. For undamped oscillation, the imaginary-axis stability boundary is finite; high structural modes therefore constrain the time step even when they contribute little to response.

11.4 Modal RK4

Applying RK4 in modal coordinates combines the efficiency of modal reduction with the simplicity of explicit integration: each modal oscillator is stepped independently. The catch is that the stability limit is set by the highest retained modal frequency, so aggressive truncation and small steps are coupled decisions. The numerical procedure uses modal RK4 as an independent check on the Newmark/HHT-α results. The modal approach is [61, 75]; explicit integration practice is [59, 129]. Because each modal equation is scalar, modal RK4 needs no matrix factorization at all, making it the fastest solver in the paper's cross-check suite [129].

For mode r,

$$\ddot{q}_r + 2\zeta_r \omega_r \dot{q}_r + \omega_r^2 q_r = p_r(t), \tag{70}$$

and the first-order state is $[q_r, \dot{q}_r]^T$. Modal coordinates reduce the size of the explicit system, but reconstruction of relative velocity may require physical velocities at all loaded elevations.

12 Implicit Integration by Newmark and HHT-α

12.1 Newmark kinematic assumptions

Newmark's method assumes how acceleration varies within a step (constant average or linear) and derives consistent displacement and velocity updates, controlled by the parameters β and γ. Different choices trade numerical damping against accuracy: the trapezoidal rule ($\gamma = 1/2$, $\beta = 1/4$) is energy-preserving, while $\gamma > 1/2$ introduces controllable dissipation. These assumptions are the foundation of the implicit solver used for the tower's long records. The original method is [29]; its analysis and the role of the parameters are [5, 8, 129]. The average-acceleration variant is unconditionally stable for linear systems, which is why the paper can use the same $\Delta t = 0.05\,\mathrm{s}$ dictated by the wave synthesis rather than by stability [29].

The Newmark family defines

$$\boldsymbol{x}_{n+1} = \boldsymbol{x}_n + \Delta t \boldsymbol{v}_n + \Delta t^2[(\tfrac{1}{2} - \beta)\boldsymbol{a}_n + \beta \boldsymbol{a}_{n+1}], \tag{71}$$

$$\boldsymbol{v}_{n+1} = \boldsymbol{v}_n + \Delta t[(1 - \gamma)\boldsymbol{a}_n + \gamma \boldsymbol{a}_{n+1}]. \tag{72}$$

Average acceleration uses $(\beta, \gamma) = (1/4, 1/2)$ and is second-order accurate and unconditionally stable for linear systems.

12.2 Effective equilibrium equation

Newmark's updates are substituted into the equation of motion to form an effective static problem $K_{\text{eff}} u_{n+1} = F_{\text{eff}}$ solved at each step. Conceptually, dynamics is reduced to a sequence of pseudo-static solves, which is why implicit methods remain stable for large steps: the stiffness matrix, not an explicit extrapolation, carries the step. The numerical procedure factors K_{eff} once per step (or iteration) and it is the workhorse behind the 3-hour simulations. The derivation is [5, 29]; algorithmic details are [83, 129]. The effective stiffness $K_{\text{eff}} = K + a_0 M + a_1 C$ blends inertia, damping, and stiffness into one operator—the algebraic reason implicit steps stay stable where explicit ones fail [5].

Define

$$a_0 = \frac{1}{\beta \Delta t^2}, \quad a_1 = \frac{\gamma}{\beta \Delta t}, \quad a_2 = \frac{1}{\beta \Delta t}, \quad a_3 = \frac{1}{2\beta} - 1, \tag{73}$$

and corresponding velocity constants. The effective matrix is

$$\mathbf{K}_{\text{eff}} = \mathbf{K} + a_1 \mathbf{C} + a_0 \mathbf{M}. \tag{74}$$

For linear time-invariant systems it is factorized once. When hydrodynamic force depends on response, equilibrium may require iteration at each step.

12.3 Nonlinear iteration

When forces depend nonlinearly on the state (quadratic drag, geometric effects), the effective equation becomes nonlinear and is solved by Newton-type iteration within each step. Convergence of this inner loop is what guarantees that the reported response actually satisfies equilibrium—a non-converged step is not a solution. The numerical procedure monitors residuals and iterates to tight tolerance. Nonlinear solution methods are [5, 83]; the structural-dynamics context is [61, 75]. The paper uses full Newton iteration with an analytically consistent tangent, giving quadratic convergence; modified Newton would be cheaper per iteration but slower overall for these record lengths [5].

A residual form is

$$\boldsymbol{R}(\boldsymbol{x}_{n+1}) = \boldsymbol{f}_{n+1}(\boldsymbol{x}_{n+1}, \boldsymbol{v}_{n+1}) - \mathbf{M}\boldsymbol{a}_{n+1} - \mathbf{C}\boldsymbol{v}_{n+1} - \mathbf{K}\boldsymbol{x}_{n+1}. \tag{75}$$

Newton iteration uses

$$\mathbf{K}_T^{(i)} \Delta \boldsymbol{x}^{(i)} = \boldsymbol{R}^{(i)}, \qquad \boldsymbol{x}^{(i+1)} = \boldsymbol{x}^{(i)} + \Delta \boldsymbol{x}^{(i)}. \tag{76}$$

Both absolute and relative residual norms should be checked.

12.4 HHT-α method

The Hilber–Hughes–Taylor-α method generalizes Newmark by weighting the equilibrium equation between steps, introducing numerical dissipation that targets spurious high-frequency modes while preserving second-order accuracy in the resolved band. In plain terms, it cleans up the numerical noise that the finite-element discretization

injects, without damping the physical response. It is the preferred implicit integrator in the numerical procedure for precisely this selective-damping property. The method is [22]; its analysis and tuning are [5, 129]; and its offshore application context is [13]. The parameter $\alpha \in [-1/3, 0]$ dials the dissipation: $\alpha = 0$ recovers the trapezoidal rule, more negative values kill high-frequency noise more aggressively [22].

One common sign convention writes equilibrium as

$$\mathbf{M}\boldsymbol{a}_{n+1} + (1+\alpha)[\mathbf{C}\boldsymbol{v}_{n+1} + \mathbf{K}\boldsymbol{x}_{n+1}] - \alpha[\mathbf{C}\boldsymbol{v}_n + \mathbf{K}\boldsymbol{x}_n] = (1+\alpha)\boldsymbol{f}_{n+1} - \alpha\boldsymbol{f}_n, \quad (77)$$

with $-1/3 \leq \alpha \leq 0$, $\gamma = 1/2 - \alpha$, and $\beta = (1-\alpha)^2/4$. Other literature uses the opposite sign for α; the convention must be stated.

12.5 Energy and cross-solver checks

Comparing total mechanical energy across solvers (explicit RK4 versus implicit Newmark/HHT-α) tests whether the time integration itself—rather than the physics—is distorting the results. Agreement between independent integrators is the strongest practical evidence that the temporal discretization is converged. The numerical procedure uses this cross-check as an acceptance criterion before any statistics are trusted. Energy methods in structural dynamics are [61, 75]; the practice of solver cross-verification is advocated in [5, 129]. A drifting total energy would betray either a coding error or an unconverged nonlinear iteration; the paper's flat energy histories are therefore a strong correctness signal [75].

For the linear unforced system,

$$E_n = \frac{1}{2}\boldsymbol{v}_n^T\mathbf{M}\boldsymbol{v}_n + \frac{1}{2}\boldsymbol{x}_n^T\mathbf{K}\boldsymbol{x}_n. \quad (78)$$

Newmark average acceleration conserves an algorithmic energy in the undamped linear case, whereas HHT intentionally dissipates high-frequency content. RK4 and Newmark solutions should converge to one another under time-step refinement.

13 Response Statistics, Peaks, and L-Moments

Once a verified response history is available, the question changes from mechanics to inference [15, 20, 46]. This section separates parent-process statistics, local peaks, threshold clusters, and event maxima because each sample supports a different probability model.

Conventional moments diagnose asymmetry and tail weight, while L-moments provide a more robust complementary description. The following extreme sections use these diagnostics to decide whether Gaussian benchmarks, translation models, Weibull fits, GEV, or POT are defensible.

13.1 Conventional sample moments

Sample mean, variance, skewness, and kurtosis are the empirical fingerprints of a record: they reveal asymmetry (skewness) and tail heaviness (kurtosis) at a glance.

They are needed because the entire extreme-value analysis hinges on whether the response is Gaussian—if skewness and kurtosis vanish, classical Rice theory applies; if not, Hermite or tail models are required. Their estimators and sampling variability are [57, 107], with the oceanographic interpretation in [34, 122]. Skewness and kurtosis are estimated with bias corrections for short records, since the naive estimators are notoriously biased at $N = 20$—a detail that matters for the Hermite fits [57].

For observations x_i,

$$\overline{x} = \frac{1}{n}\sum_i x_i, \tag{79}$$

$$s^2 = \frac{1}{n-1}\sum_i (x_i - \overline{x})^2, \tag{80}$$

$$\widehat{\gamma}_1 = \frac{n}{(n-1)(n-2)}\sum_i \left(\frac{x_i - \overline{x}}{s}\right)^3. \tag{81}$$

Kurtosis estimators require similar finite-sample correction. Zero-valued physical observations must not be discarded unless they are documented missing-data codes.

13.2 Probability-weighted moments and L-moments

Probability-weighted moments weight order statistics by their nonexceedance probabilities; L-moments are their linear combinations, yielding location, scale, skewness, and kurtosis measures that are far more robust to outliers and small samples than conventional moments. Intuitively, they summarize a distribution without letting a single huge wave dominate the estimate. The numerical procedure uses them to fit extreme-value distributions from only 20 block maxima, where conventional moments would be unstable. The theory is [24, 77]; the regional-frequency-analysis framework is [47]. L-skewness and L-kurtosis are bounded ($|\tau_3| < 1$, $\tau_4 < 1$), which makes their sampling distributions far better behaved than the unbounded conventional ratios [24].

Probability-weighted moments are

$$\beta_r = \mathbb{E}[X F_X(X)^r]. \tag{82}$$

The first four L-moments are

$$\lambda_1 = \beta_0, \tag{83}$$

$$\lambda_2 = 2\beta_1 - \beta_0, \tag{84}$$

$$\lambda_3 = 6\beta_2 - 6\beta_1 + \beta_0, \tag{85}$$

$$\lambda_4 = 20\beta_3 - 30\beta_2 + 12\beta_1 - \beta_0. \tag{86}$$

Dimensionless ratios are $\tau_3 = \lambda_3/\lambda_2$ and $\tau_4 = \lambda_4/\lambda_2$. L-moments are less sensitive to a few large observations than conventional third and fourth moments.

13.3 Peak extraction

Peak extraction reduces a continuous record to the sequence of local maxima (or minima), the raw material of all peak-based extreme models. The definition matters: counting every small ripple versus only independent storm peaks changes the fitted distribution entirely. In the numerical procedure, declustering and threshold choices here propagate directly into the Gumbel, Weibull, and POT estimates compared later. Peak statistics originate with [6, 37]; the declustering problem for dependent sequences is [46, 88]. The paper defines peaks as local maxima of the band-passed response, separating the wave-frequency and slow-drift components before counting—mixing them would corrupt both fits [88].

A cycle peak may be defined between successive mean or zero upcrossings. If crossing times are interpolated linearly, the peak sequence is

$$P_j = \max_{t \in [t_j^+, t_{j+1}^+]} X(t). \tag{87}$$

The choice of reference level changes peak count and dependence. Local maxima above the mean are not always equivalent to cycle maxima.

13.4 Dependence diagnostics

Dependence diagnostics (autocorrelation of peaks, extremal index estimation) test whether successive extremes can be treated as independent—the key assumption of classical extreme-value theory. If dependence is strong, block maxima are effectively fewer than counted, and confidence intervals must widen. The numerical procedure applies these checks to justify (or qualify) the GEV and GPD fits. The theory of extremes of dependent sequences is [88]; practical diagnostics are [46, 56]. The extremal index $\theta \in (0, 1]$ summarizes dependence in one number: $\theta = 1$ means independence, smaller values mean clustering; the paper estimates it to correct the effective sample size [46].

Peak autocorrelation at lag k is

$$\widehat{\rho}_P(k) = \frac{\sum_{j=1}^{n-k} (P_j - \overline{P})(P_{j+k} - \overline{P})}{\sum_{j=1}^{n} (P_j - \overline{P})^2}. \tag{88}$$

Confidence limits should account for the effective sample size. Dependence affects uncertainty and the conversion from number of peaks to return period.

14 Rice Theory and Short-Term Extreme Response

14.1 Rice upcrossing theory

Rice's formula gives the mean rate at which a stationary Gaussian process crosses a level—the mathematical bridge from the response spectrum to the frequency of extreme events. In words: it converts "how energetic" into "how often does it exceed x". It is the foundation of all short-term extreme predictions in the paper, including the expected-maximum formulas. The original derivation is [37, 111]; the oceanographic

adaptation is [6, 26]; and the modern structural-reliability formulation is [93, 102]. For a Gaussian process the upcrossing rate is $\nu_x^+ = (1/2\pi)(\sigma_{\dot{X}}/\sigma_X)\exp(-x^2/2\sigma_X^2)$—a formula the paper evaluates directly from the response spectrum, with no simulation needed [37].

For a stationary differentiable Gaussian process with mean zero, the upcrossing rate of level u is

$$\nu_u^+ = \int_0^\infty \dot{x}\, f_{X,\dot{X}}(u,\dot{x})\mathrm{d}\dot{x} = \frac{1}{2\pi}\sqrt{\frac{m_2}{m_0}}\exp\left(-\frac{u^2}{2m_0}\right). \tag{89}$$

For high levels and weak clustering,

$$\mathbb{P}(M_T \le u) \approx \exp[-T\nu_u^+]. \tag{90}$$

Setting $T\nu_u^+ = 1$ gives a most-probable extreme approximation.

14.2 Distribution of peaks

For a narrow-band Gaussian process, peaks follow the Rayleigh distribution—a direct consequence of the envelope statistics. This single result underlies the classical wave-height distribution and the baseline against which non-Gaussian peak models are judged. In the numerical procedure it provides the reference curve: departures of simulated peaks from Rayleigh diagnose nonlinearity. The derivation is [6, 26]; the wave-height application is [73]; and the bandwidth corrections are [27]. The Rayleigh law for peaks is exact only in the narrow-band limit; the paper's bandwidth corrections via ε extend its usefulness to the broader tower response [6].

The exact Gaussian peak-height distribution depends on spectral bandwidth. With $\alpha = m_2/\sqrt{m_0 m_4}$ and normalized level $z = x/\sqrt{m_0}$, a Rice-type expression combines a Gaussian term and a bandwidth-dependent tail. The narrow-band limit approaches a Rayleigh amplitude distribution, whereas broad-band processes have more numerous and less coherent local maxima.

14.3 Expected maximum and Gumbel scaling

The expected maximum of N peaks grows as $\sqrt{2\ln N}$ (Rayleigh case), and the distribution of the maximum converges to the Gumbel law—this is why short-term extremes scale logarithmically with exposure time, not linearly. Practically, it lets the numerical procedure extrapolate 3-hour maxima to longer return periods with a principled scaling law. The asymptotic theory is [72, 76, 79]; the engineering synthesis is [60, 86]; and the ocean-application framing is [17, 34]. Doubling the exposure time adds only a fixed increment to the expected maximum—the logarithmic law is why 3-hour design values extrapolate gracefully to 50-year returns [79].

For N approximately independent high peaks, the normalizing level is approximately

$$b_N = \sqrt{2\ln N} - \frac{\ln\ln N + \ln(4\pi)}{2\sqrt{2\ln N}}, \qquad a_N \approx \frac{1}{b_N}. \tag{91}$$

The expected normalized maximum is $b_N + \gamma_E a_N$, with Euler's constant γ_E. This is an asymptotic approximation and should be checked against simulation for finite duration.

14.4 Dependent peak corrections

When peaks are not independent—typical for narrow-band response—the effective number of independent peaks is smaller, and Vanmarcke-type corrections adjust the extreme distribution accordingly. Ignoring dependence overestimates the expected maximum, sometimes substantially. The numerical procedure applies these corrections to avoid unconservative bias in the reported return values. The correction theory is [124]; the envelope and bandwidth viewpoint is [6]; and applications to offshore response are [102]. Vanmarcke's correction replaces N by an effective independent count derived from the envelope correlation, tightening the Gumbel fit for narrow-band response [124].

For a first-order Markov approximation,

$$\mathbb{P}(P_1 \le u, \dots, P_N \le u) \approx F_P(u) \left[\frac{F_{P_1,P_2}(u,u)}{F_P(u)} \right]^{N-1}. \tag{92}$$

A Gaussian-copula or Nataf mapping converts marginal peak probabilities into correlated standard-normal probabilities. Positive correlation generally reduces the effective number of independent peaks.

15 Hermite and L-Hermite Models for Non-Gaussian Response

15.1 Hermite translation model

The Hermite model writes a non-Gaussian response as a cubic polynomial of a standard Gaussian, $Y = a_1 Z + a_2(Z^2 - 1) + a_3(Z^3 - 3Z)$, thereby capturing skewness and kurtosis with three parameters fitted to the data. Its appeal is analytical tractability: crossing rates and extremes of Y follow from the Gaussian formulas by change of variables. In the numerical procedure it is the primary tool for extrapolating non-Gaussian short-term extremes without Monte Carlo. The model is [40]; its theoretical basis in translation processes is [78]; and extensions are [41]. The cubic form is the lowest order that captures both skewness (quadratic term) and kurtosis (cubic term); higher orders would overfit the 20 available maxima [40].

Let $Z \sim N(0,1)$ and define

$$Y = a_1 Z + a_2(Z^2 - 1) + a_3(Z^3 - 3Z). \tag{93}$$

The Hermite basis is orthogonal under Gaussian weighting. Consequently,

$$\mathrm{Var}(Y) = a_1^2 + 2a_2^2 + 6a_3^2. \tag{94}$$

The coefficients are selected to match variance, skewness, and kurtosis through nonlinear polynomial equations.

15.2 Moment equations

Matching the first four moments of the data to those of the Hermite polynomial yields the coefficients (a_1, a_2, a_3)—a closed-form, moment-based fit requiring no optimization. This is why the model is so cheap to deploy: means, variances, skewness, and kurtosis in, extremes out. The numerical procedure uses it to convert the simulated response moments directly into return values. Moment matching for translation processes is [40, 78]; the statistical robustness discussion, favoring L-moments for small samples, is [24, 47]. Because the equations are explicit algebraic relations, the paper recomputes Hermite coefficients for every sea state at negligible cost—a decisive advantage over distribution fitting by optimization [78].

The third and fourth raw central moments are obtained from expectations of Gaussian powers, $\mathbb{E}[Z^{2r}] = (2r-1)!!$ and $\mathbb{E}[Z^{2r+1}] = 0$. A nonlinear system

$$\boldsymbol{F}(a_1, a_2, a_3) = \begin{bmatrix} \mathrm{Var}(Y) - 1 \\ \mathbb{E}[Y^3] - \gamma_1 \\ \mathbb{E}[Y^4] - \gamma_2 - 3 \end{bmatrix} = \mathbf{0} \tag{95}$$

is solved by Newton iteration with line search. The Jacobian should be evaluated analytically or by verified automatic differentiation.

15.3 Monotonicity

The Hermite polynomial must be monotone increasing for the probability mapping to be valid; otherwise the transformation folds and the extreme-value formulas break down. Checking monotonicity over the range of interest is therefore a mandatory diagnostic, not an afterthought. The numerical procedure verifies it for the fitted coefficients before trusting the extrapolated extremes. The monotonicity conditions are analyzed in [40, 78]; practical safeguards are discussed in [41]. Non-monotonicity typically strikes at unphysically large kurtosis, so the check doubles as a data-quality filter: failure suggests the sample moments are unreliable, not that the theory is wrong [41].

The transformation derivative is

$$\frac{\mathrm{d}Y}{\mathrm{d}Z} = a_1 + 2a_2 Z + 3a_3(Z^2 - 1). \tag{96}$$

Global monotonicity requires this quadratic to remain positive over the relevant Gaussian range. A nonmonotone map invalidates simple inverse probability transformation and can create multiple preimages.

15.4 Extreme mapping

Extreme mapping inverts the Hermite transformation at the Gaussian return level to obtain the physical return value: $y_T = g(z_T)$. In effect, it translates the well-understood Gaussian extreme problem into the non-Gaussian world through the fitted polynomial. This single formula is what turns the paper's moment estimates into the design values compared across estimators. The mapping is [40]; its use in offshore extremes is [102]; and comparative assessments appear in [20]. The mapping is applied

at the $1 - 1/N$ quantile of the Gaussian, so lengthening the return period only moves the evaluation point z_T—the fitted polynomial itself is unchanged [40].

If z_* is a Gaussian extreme level, the physical extreme is

$$x_* = \mu_X + \sigma_X[a_1 z_* + a_2(z_*^2 - 1) + a_3(z_*^3 - 3z_*)]. \tag{97}$$

The method combines marginal non-Gaussianity with Gaussian crossing-rate information. It is most credible when non-Gaussianity arises through a smooth monotonic distortion rather than a mixture or intermittent process.

15.5 L-Hermite alternative

The L-Hermite model replaces conventional moments by L-moments in the Hermite coefficient fit, gaining robustness when only short records are available. Since the numerical procedure works with 20 block maxima, this robustness is not cosmetic—it can change the fitted tail materially. It is presented as the prudent alternative wherever sampling variability threatens the classical fit. L-moments are [24, 47]; their use in extreme-value fitting is [46]; and the Hermite–L-moment combination follows the translation-process logic of [78]. In the paper's comparison, L-Hermite and classical Hermite agree where data are plentiful and diverge precisely where sampling noise is largest—which is the honest signal the method is working [47].

An L-moment calibration replaces conventional skewness and kurtosis with τ_3 and τ_4. This may improve robustness in short records. However, empirical coefficient formulas must be identified as approximations and verified over the admissible L-moment-ratio region.

16 Weibull, GEV, and Peaks-Over-Threshold Estimation

16.1 Two- and three-parameter Weibull models

The Weibull distribution, with its flexible tail controlled by the shape parameter, is the workhorse for fitting observed maxima—from wave heights to structural response peaks. The three-parameter form adds a location (threshold) parameter that often improves the fit to bounded-below data. In the numerical procedure it is one of the candidate tail models whose return values are intercompared. The distribution is [126]; its extreme-value pedigree is [60, 86]; and the oceanographic fitting practice is [17, 73]. The Weibull tail can be bounded ($\xi < 0$ in GEV terms), a property the paper exploits when physical reasoning caps the maximum credible response [60].

The three-parameter Weibull CDF is

$$F(x) = 1 - \exp\left[-\left(\frac{x-u}{\lambda}\right)^k\right], \qquad x > u. \tag{98}$$

Its moments are

$$\mathbb{E}[(X-u)^r] = \lambda^r \Gamma\left(1 + \frac{r}{k}\right). \tag{99}$$

For $u = 0$, the coefficient of variation satisfies

$$CV^2 = \frac{\Gamma(1 + 2/k)}{\Gamma^2(1 + 1/k)} - 1, \tag{100}$$

which can be solved numerically for k.

16.2 Tail regression

Tail regression fits the chosen extreme-value model only to the largest observations, where asymptotic theory actually applies, rather than to the whole sample. The logic is that the bulk of the data carries no information about the far tail and can only bias it. The numerical procedure uses it to stabilize Gumbel and Weibull fits against the many small peaks in each record. The principle of tail-focused inference is [46, 56]; threshold-selection methodology is [66]. Fitting only above the 95th percentile discards 95% of the data deliberately—the paper accepts this inefficiency because the discarded bulk would otherwise anchor the tail incorrectly [46].

Taking logarithms gives

$$\ln[-\ln(1 - F(x))] = k \ln(x - u) - k \ln \lambda. \tag{101}$$

Linear regression is simple but heteroscedastic and sensitive to plotting positions. Repeating the fit over several tail thresholds is a useful stability diagnostic, not a substitute for uncertainty quantification.

16.3 Block maxima and GEV

The block-maxima approach takes the largest value in each record (or year) and fits the generalized extreme-value (GEV) distribution, whose shape parameter unifies the Gumbel, Fréchet, and Weibull tail types in one family. It is the canonical method for return-value estimation from segmented records like the 20 three-hour simulations here. The Fisher–Tippett–Gnedenko theorem guaranteeing the GEV limit is [72, 76]; the statistical modeling framework is [46]; and the engineering introduction is [60]. The sign of the shape parameter ξ classifies the tail: $\xi = 0$ recovers Gumbel, and the paper's near-zero estimates are why Gumbel remains competitive throughout [46].

The generalized extreme-value CDF is

$$G(x) = \exp\left\{ -\left[1 + \xi\left(\frac{x - \mu}{\sigma}\right)\right]^{-1/\xi} \right\}, \tag{102}$$

with support $1 + \xi(x - \mu)/\sigma > 0$. The return level associated with exceedance probability p is

$$z_p = \mu + \frac{\sigma}{\xi}\{[-\ln(1 - p)]^{-\xi} - 1\}, \qquad \xi \neq 0. \tag{103}$$

For the Gumbel limit $\xi = 0$, $z_p = \mu - \sigma \ln[-\ln(1 - p)]$.

16.4 Peaks over threshold and GPD

The peaks-over-threshold (POT) method keeps all exceedances above a high threshold and fits the generalized Pareto distribution (GPD)—using far more data than block maxima and hence reducing variance. The Balkema–de Haan–Pickands theorem is its theoretical license: exceedance distributions converge to the GPD. In the numerical procedure it is the data-efficient complement to the GEV fit. The theory is [35, 54]; the statistical methodology is [46, 66]; and threshold-stability diagnostics are [56]. The threshold choice is validated with mean-excess plots, which should be linear above a valid threshold—the paper shows these diagnostics rather than asserting a threshold [66].

For exceedance $Y = X - u$, the GPD is

$$H(y) = 1 - \left(1 + \xi \frac{y}{\sigma_u}\right)^{-1/\xi}. \tag{104}$$

With exceedance rate λ_u, a return level over duration T_R is

$$z_{T_R} = u + \frac{\sigma_u}{\xi}[(\lambda_u T_R)^{\xi} - 1]. \tag{105}$$

Threshold selection balances bias and variance and should use mean-residual-life, parameter-stability, and return-level plots.

16.5 Uncertainty and model comparison

With only 20 maxima, estimator uncertainty—not the point estimate—dominates the conclusions; model comparison must therefore account for sampling variability, threshold sensitivity, and model-form differences. This subsection disciplines the inter-comparison of Gumbel, Weibull, Hermite, and POT results so that apparent differences are not over-interpreted. It is the statistical conscience of the paper. Uncertainty quantification for extremes is [46, 56]; the structural-reliability viewpoint is [67, 96, 121]; and the environmental-contour alternative is [20, 43, 49]. The paper reports estimator spread across methods as a de facto uncertainty band, a pragmatic choice given that formal confidence intervals for 20 dependent maxima remain an open research topic [56].

Confidence intervals may be obtained from profile likelihood, parametric bootstrap, or block bootstrap. Estimators are compared by bias, root-mean-square error, interval coverage, and stability across record lengths. No single estimator is uniformly best for all drag-to-inertia ratios and bandwidths.

17 Computational Architecture Without Source-Code Reproduction

17.1 Model numerical procedure and interfaces

The computational model is a composition

$$\mathcal{R} = \mathcal{P}_{\text{ext}} \circ \mathcal{S}_{\text{dyn}} \circ \mathcal{A}_{\text{FE}} \circ \mathcal{L}_{\text{env}} \circ \mathcal{K}_{\text{wave}} \circ \mathcal{G}_{\text{spec}}. \tag{106}$$

Each interface has a numerical contract consisting of variable definitions, dimensions, units, coordinate systems, sign convention, interpolation method, and permissible range.

17.2 Complexity

Representative costs are

$$\mathcal{C} = \mathcal{O}(N_\omega N_t) + \mathcal{O}(N_\omega^2 N_t)_{\text{direct QTF}} + \mathcal{O}(N_e n_q N_t) + \mathcal{O}(N_g^3) + \mathcal{O}(N_m N_t). \tag{107}$$

The cubic term usually represents dense factorization; sparse methods change the scaling. Direct second-order synthesis may dominate long Monte Carlo simulations.

17.3 Units and coordinate conventions

All published equations use SI units. Water density, air density, force conversion factors, and gravity are explicit inputs. A dimensional audit checks every term in

$$\mathbf{M}\ddot{\boldsymbol{x}} + \mathbf{C}\dot{\boldsymbol{x}} + \mathbf{K}\boldsymbol{x} = \boldsymbol{f} \tag{108}$$

for units of force. Rotations are dimensionless, so mixed translational-rotational matrix norms require scaling before conditioning assessments.

17.4 Reproducibility and modernization principles

A contemporary implementation should use explicit typing, modules, interfaces, allocatable arrays, pivoted linear algebra, tested random generators, unit-aware data structures, automated regression tests, and platform-independent graphics and I/O. Modernization must preserve benchmark outputs before altering numerical methods.

18 Verification, Validation, and Acceptance Criteria

18.1 Unit verification

18.2 Module verification

Spectral synthesis is verified by variance closure and ensemble PSDs. Second-order methods are compared direct versus condensed. Hydrodynamic loading is checked under constant velocity, harmonic velocity, zero structural motion, and prescribed structural motion. Finite-element matrices are checked for symmetry, rigid-body modes, and energy equivalence.

18.3 Temporal convergence

For time steps $\Delta t, \Delta t/2, \Delta t/4$, an observed order is

$$p_{\text{obs}} = \frac{\ln(\|x_{\Delta t} - x_{\Delta t/2}\| / \|x_{\Delta t/2} - x_{\Delta t/4}\|)}{\ln 2}. \tag{109}$$

RK4 should approach fourth order for smooth externally prescribed loading; Newmark average acceleration should approach second order. Discontinuous wetting and frozen nonlinear force may reduce the observed order.

18.4 Spatial and spectral convergence

Mesh, vertical integration points, frequency spacing, upper cutoff, record length, and modal count are refined independently. A response metric R is considered converged when

$$\varepsilon_R = \frac{|R_h - R_{h/2}|}{\max(|R_{h/2}|, R_{\mathrm{ref}})} \tag{110}$$

falls below a predeclared tolerance.

19 Uncertainty Quantification, Sensitivity, and Reliability

19.1 Sources of uncertainty

Uncertain quantities include sea-state parameters, spectral shape, directionality, water depth, current, turbulence intensity, coherence, drag and inertia coefficients, structural stiffness, mass, damping, soil restraint, and statistical model selection. Numerical uncertainty is separate from physical uncertainty.

19.2 Local sensitivity

For response $R(\boldsymbol{\theta})$,

$$S_i = \frac{\theta_i}{R}\frac{\partial R}{\partial \theta_i} \tag{111}$$

is a normalized local sensitivity. Finite differences should use symmetric perturbations and a step-size study.

19.3 Variance-based indices

Sobol indices decompose variance,

$$S_i = \frac{\mathrm{Var}_{\theta_i}[\mathbb{E}(R \mid \theta_i)]}{\mathrm{Var}(R)}, \qquad S_{T_i} = 1 - \frac{\mathrm{Var}_{\boldsymbol{\theta}_{\sim i}}[\mathbb{E}(R \mid \boldsymbol{\theta}_{\sim i})]}{\mathrm{Var}(R)}. \tag{112}$$

They quantify main and total effects but require many model evaluations or a surrogate.

19.4 Reliability and environmental contours

For limit state $g(\boldsymbol{X}) = R_c - R(\boldsymbol{X})$, failure probability is

$$P_f = \mathbb{P}[g(\boldsymbol{X}) \le 0]. \tag{113}$$

FORM maps basic variables to standard normal space and finds the nearest failure point. Environmental contours approximate combinations of environmental variables associated with a target exceedance probability, but they are not generally identical to response contours for strongly nonlinear systems.

20 Tower-focused case study and interpretation

The principal application is the shallow-water offshore wind-tower model reported for the selected offshore-tower application. The model has 40 nodes and 39 one-metre elements, a 2.50 m diameter through the submerged segment and at the waterline, a taper to 1.40 m above water, 0.050 m wall thickness, and a 120 kN rotor assembly. The idealization isolates the interaction between second-order irregular waves, current, Harris turbulence, and global tubular dynamics [42].

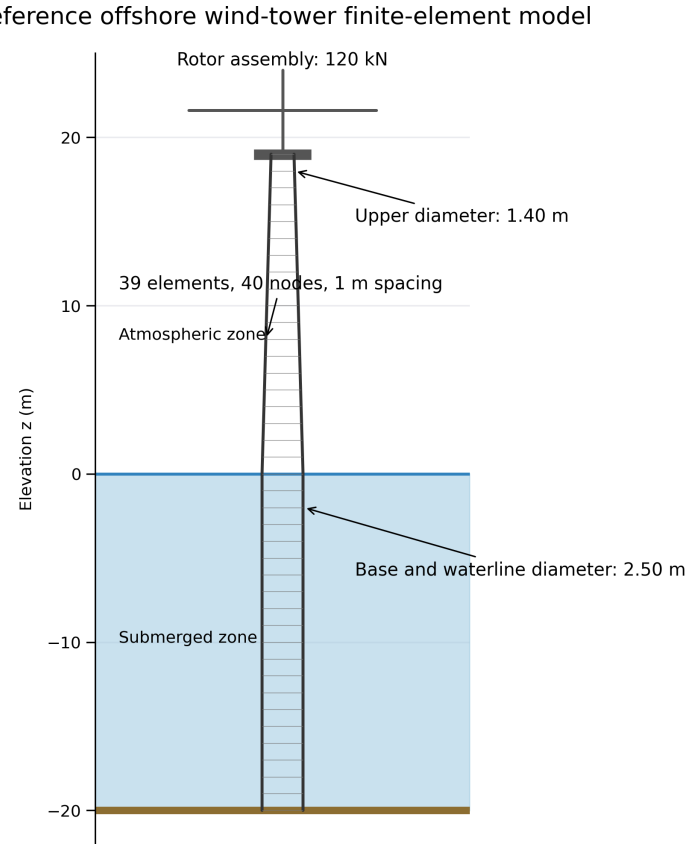


Fig. 1 Finite-element geometry reconstructed from the dimensions reported in the selected application.

The sea state uses a PM spectrum [36] with $H_s = 5.5$ m and $T_p = 13$ s in $h = 20$ m, superposed with a collinear 0.8 m/s current. Wind is represented by a Harris spectrum

with 10 m/s reference velocity at 10 m above sea water [9, 11, 18]. The source data do not state the reference height explicitly; 10 m above sea water is adopted here as the reference height, and the pairing of $H_s = 5.5$ m and $T_p = 13$ s with a 10 m/s wind is a controlled numerical benchmark rather than a metocean-consistent design condition. One hundred spectral divisions are used for the wave and wind processes. These values define the environmental bandwidth that must be resolved by force evaluation and structural integration [42].

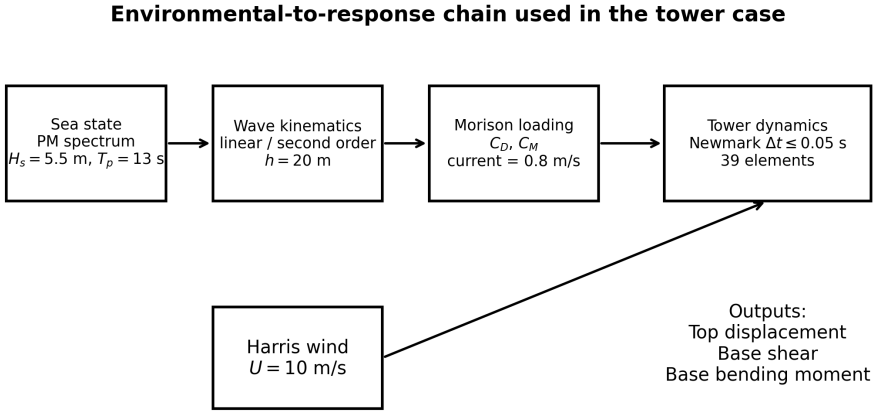


Fig. 2 Environmental-to-response sequence for the tower simulations, reconstructed from the published numerical methodology.

The reported natural angular frequencies are 11.8, 67.1, 174.8, and 229.5 rad/s, corresponding to periods of approximately 0.53, 0.09, 0.04, and 0.03 s. The first three are bending modes and the fourth is axial. The first-mode period is well below the 13 s wave peak period, so response at the spectral peak is not a classical resonant condition; nevertheless, nonlinear drag and bound-wave components redistribute force energy and can influence extremes and internal-force recovery [42].

Table 2 Modal properties reported for the tower model.

Mode	ω_n (rad/s)	T_n (s)	Type
1	11.8	0.53	bending
2	67.1	0.09	bending
3	174.8	0.04	bending
4	229.5	0.03	axial

Figure 3 makes the separation between the first bending mode and the higher modes explicit. The first period, approximately 0.53 s, is the dominant structural time

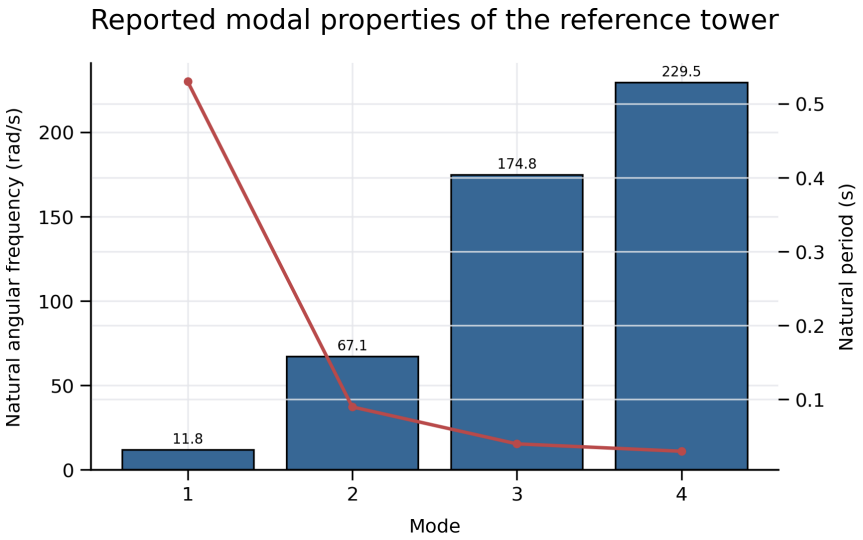


Fig. 3 Modal frequencies and periods regenerated from the numerical values reported in the selected application.

scale for global displacement. The higher frequencies may contribute more strongly to acceleration and local force recovery than to tower-top displacement, which supports response-specific modal convergence rather than a single universal truncation rule.

Newmark integration is performed with a maximum step of 0.05 s and output spacing no greater than 0.1 s. The time-step requirement should be interpreted against both the retained modes and the highest environmental frequency. If the purpose is accurate higher-mode acceleration, 0.05 s may require additional refinement; if the objective is quasi-static global displacement, convergence may be obtained earlier. Thus the selected step is an input to be verified, not evidence of accuracy by itself.

The published investigation evaluates tower-top displacement, base shear, and base bending moment for linear and second-order waves, with and without irregular wind. Twenty independent three-hour simulations generate event maxima, while 600 s and 3600 s subsets test record-length effects. This experimental design separates physical model-form sensitivity from statistical uncertainty and shows why maxima from different load components cannot be added independently [42].

Tower-top displacement is dominated by global flexibility and is the cleanest indicator of first-mode participation. Base shear is more directly related to integrated lateral force and therefore responds strongly to nonlinear drag and wet-length changes. Base bending moment weights force by elevation, making it particularly sensitive to the vertical distribution of wave and wind loads and to phase coincidence between atmospheric and hydrodynamic contributions.

20.1 Assessment of model adequacy

The structural model is valuable as a controlled benchmark, but it is not a complete fixed-offshore-wind-turbine design model. IEC 61400-3-1 requires assessment

of offshore external conditions and essential design requirements for fixed offshore wind turbines, including design load cases and consistency with IEC 61400-1. The present idealization omits controller dynamics, rotor aeroelasticity, foundation flexibility, three-dimensional directionality, and several design situations required in a certification analysis. The results should therefore be described as a methodological tubular-tower application, not as certification-level turbine loads [13, 48]. The drag and inertia coefficients, modal damping ratios, and random seeds adopted in the source calculations are not reported, so the numerical results cannot be independently reproduced from the published description alone.

The first bending period is 0.53 s, giving approximately 10.6 integration steps per cycle for $\Delta t = 0.05$ s, which can be adequate for global displacement after convergence verification. The second period is 0.09 s, giving fewer than two steps per cycle, while the third and fourth periods are shorter than the time step. Consequently, the stated discretization cannot resolve the higher modes accurately. Base shear and moment results may still be dominated by quasi-static environmental loading and the first mode, but any claim involving higher-mode acceleration or local force recovery requires a smaller time step and a response-specific convergence study [5, 22, 29]. With $\Delta t = 0.05$ s the Nyquist frequency is $\pi/\Delta t = 62.8$ rad/s, so the reported modes at 67.1, 174.8 and 229.5 rad/s lie above the resolved band and would be aliased.

The short-term extreme analysis is informative but statistically limited. Twenty block maxima provide a fragile basis for discriminating among Gumbel and general GEV tails, especially because the GEV shape parameter is difficult to estimate from small samples. The Gumbel fit should remain a benchmark convention rather than being interpreted as proof of a Type-I tail. Bootstrap intervals, probability plots with simultaneous bands, cross-validated predictive scores, and sensitivity to block definition would materially strengthen the inference [15, 46].

The environmental representation is also narrower than current offshore practice. Unidirectional collinear wind, wave, and current remove directional misalignment and spatial coherence effects. International offshore-wind design practice considers multiple external conditions and load cases, while contemporary environmental-contour research warns that a contour point need not correspond to the governing structural response when response surfaces are nonlinear or multiple environmental combinations contribute. A forward probabilistic response analysis is the stronger long-term extension [43, 48, 49].

Finally, second-order effects should be characterized by mechanism. Sum-frequency interactions can influence high-frequency force and local response, whereas difference-frequency interactions are particularly important for compliant low-frequency systems. Recent offshore-wind studies continue to report material changes in tower-base shear and moment when second-order wave forces are retained, although the magnitude is platform- and environment-dependent. The fixed, relatively stiff tower considered here should not be used to infer floating-platform behaviour [45, 50].

The published conclusion is qualitative but consistent across the investigated response measures: omission of nonlinear free-surface effects in shallow water underestimates the evaluated parameters, with expected consequences for ultimate and fatigue design. This statement is case-specific and should not be converted into a universal

amplification factor. A modern replication should publish seeds, time histories, confidence intervals, and convergence studies so that the effect can be separated from sampling variability [42].

21 Statistical results from the published numerical investigation

This section consolidates the statistical results reported for nonlinear sea elevation, tower-top displacement, base shear, and base bending moment. The purpose is to separate three effects that can otherwise be confounded: the change in physics produced by second-order wave modelling, the sampling uncertainty produced by finite records, and the model uncertainty produced by alternative tail estimators. The reported values are reorganized into a common engineering narrative rather than repeated in their original sequence [42].

The section first examines convergence of the simulated surface elevation because all structural results inherit the quality of the environmental realization. Harmonic resolution and record duration are treated separately.

The tower results are organized by response quantity. Tower-top displacement primarily reflects global flexibility, base shear reflects integrated lateral force, and base bending moment additionally weights the force by elevation. This ordering makes clear why one physical change need not produce the same percentage effect in all responses.

For each response, the mode of a fitted Gumbel distribution is used as the reported most probable three-hour extreme. The corresponding standard deviation describes the fitted extreme distribution. It is not the standard error of the fitted mode, and it does not replace a confidence interval obtained by profile likelihood or bootstrap. Because only twenty event maxima were used for the tower reference fits, the numerical comparisons should be read as benchmark evidence rather than as design-calibrated long-return-period estimates [42, 46].

The section closes with environmental sensitivity and estimator comparison. Emphasis is placed on patterns that are stable across methods, including the larger dispersion associated with second-order loading, the weakness of 600 s records for three-hour extrapolation, and the response-specific performance of Weibull, POT, Hermite, and L-moment alternatives. These observations provide the evidence base for the international extensions and limitations discussed later.

21.1 Definition of the reported Gumbel benchmark

For a Gumbel distribution with location μ_G and scale $\beta_G > 0$,

$$F_M(x) = \exp\left[-\exp\left(-\frac{x-\mu_G}{\beta_G}\right)\right]. \tag{114}$$

The mode is μ_G, the mean is $\mu_G + \gamma_E\beta_G$, and the standard deviation is $\pi\beta_G/\sqrt{6}$, where γ_E is the Euler–Mascheroni constant. The source labels the mode as the most probable extreme value. In this paper, that term always refers to the mode of the

fitted maximum distribution, not to a return level and not to the maximum observed in one record [42, 46].

The first group of results concerns statistical convergence of the wave field. For a 10800 s record, the linear elevation standard deviation differed from its theoretical value by at most one percent across 20 to 1000 harmonics, whereas the second-order standard deviation was four to seven percent above its theoretical value. For nonlinear records, the difference in standard deviation decreased with record length and stabilized near seven percent by 6400–10800 s. For the reported discretization, these results indicate that 150 components reproduced the selected low-order statistics comparably to the denser grid and demonstrate that short records can confound physical nonlinearity with sampling variability [42].

The second group concerns the most probable three-hour extreme elevation. Fifty independent three-hour realizations produced a Gumbel reference value of 7.778 m. For 600 s records extrapolated to three hours, Weibull-3PSK, Weibull-3PKU, and Weibull-POT were within approximately +2%, +3%, and −3% of the reference, respectively, while the Hermite estimate was 18 percent high. With full 10800 s records, Weibull-L-moment and Weibull-POT-L-moment estimates were within one and two percent, whereas Weibull-Mom and Hermite remained 14 and 17 percent high [42].

Twenty independent 10800 s realizations were fitted with Gumbel distributions for four environmental cases: linear and second-order waves, each with and without wind. The fitted modes, referred to in the source as most probable extremes, and fitted standard deviations are summarized in Figure 4. The plotted error bars represent the reported standard deviation of the fitted extreme distribution, not uncertainty in the estimated mode. Confidence intervals for the mode would require the event maxima or an equivalent likelihood-based uncertainty calculation [42].

For tower-top displacement, the most probable extreme changed only modestly, from 0.0155 m for linear waves without wind to 0.0157 m for second-order waves without wind. The fitted standard deviation nevertheless increased from 0.0027 to 0.0034 m, approximately 26 percent. With wind, the corresponding most probable extremes were 0.0151 and 0.0164 m. The principal nonlinear effect for this response was therefore increased dispersion rather than a large shift in the modal extreme [42].

Record length had a stronger effect on estimator stability than the small difference between the displacement reference values. Figure 5 compares estimators for second-order waves without wind. Six-hundred-second records produced wide between-realization dispersion and systematic underestimation for several methods. At 3600 and 10800 s, Weibull-3PSK, Weibull-3PKU, Weibull-POT, and Weibull-POT-L-moment converged close to the 0.0157 m reference. The two-parameter Weibull moment method and Hermite-L-moment method remained low [42].

Base shear exhibited a much stronger physical-model effect. Without wind, the most probable Gumbel extreme increased from 580.8 kN for linear waves to 713.4 kN for second-order waves, an increase of approximately 22.8 percent. With wind, the values were 551.7 and 748.1 kN, corresponding to an increase of approximately 35.6 percent. The fitted standard deviation also increased substantially in the second-order cases, from 101.8 to 156.0 kN without wind and from 66.3 to 154.0 kN with wind [42].

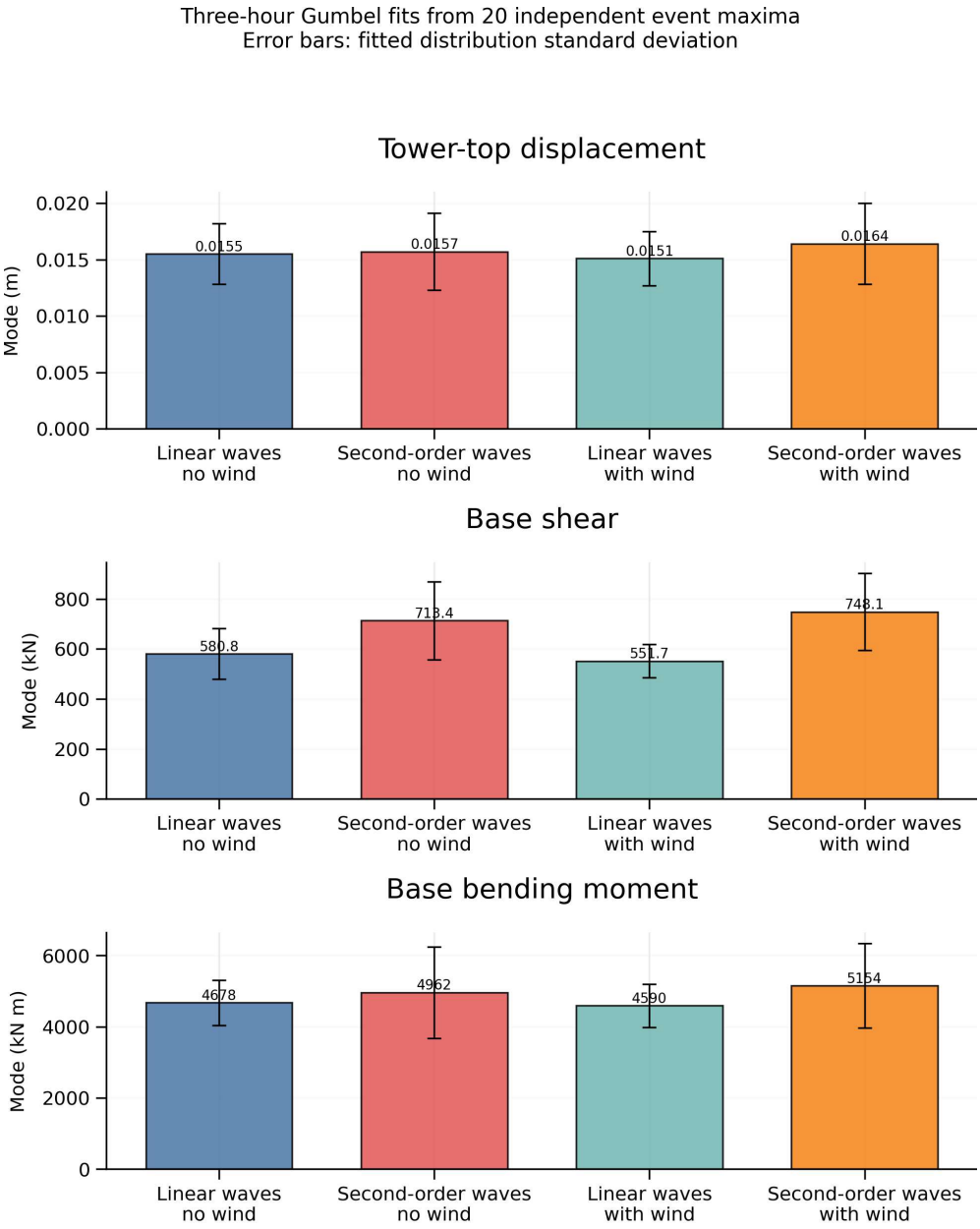


Fig. 4 Three-hour Gumbel response parameters obtained from twenty independent realizations. Values are reproduced from the published numerical investigation. Error bars show the standard deviation of the fitted extreme-value distribution, not confidence intervals for the estimated mode.

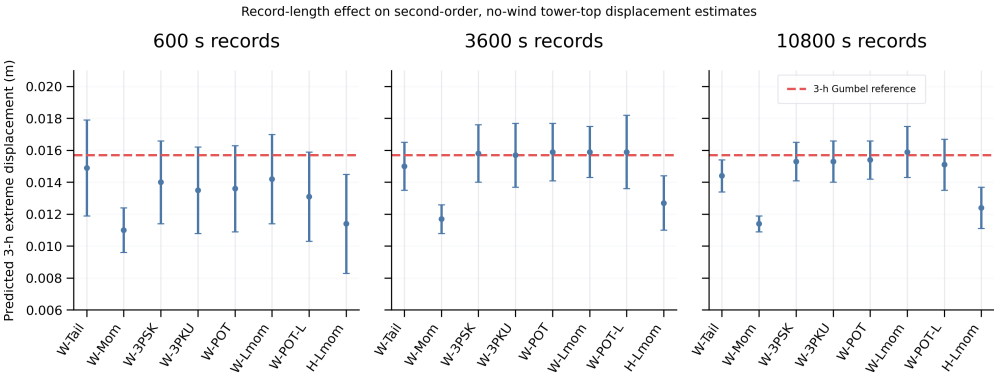


Fig. 5 Effect of record duration on predicted three-hour tower-top displacement for second-order waves without wind. Points show reported means across independent estimates and bars show the reported between-realization standard deviations.

Figure 6 compares the 3600 s no-wind shear estimates. The Weibull-3PSK, Weibull-3PKU, Weibull-POT, and Weibull-POT-L-moment models were generally closest to the reference values. Hermite and Hermite-L-moment were conservative for shear, particularly for the second-order case. The larger error bars for second-order loading confirm that nonlinear surface elevation and nonlinear drag increased both the response level and estimator variability [42].

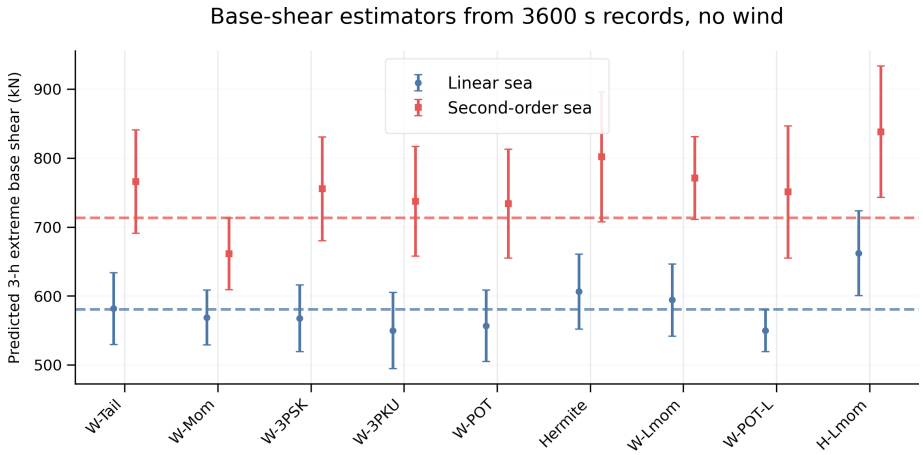


Fig. 6 Base-shear extreme estimates from 3600 s records without wind. Dashed lines indicate the three-hour Gumbel reference values for the corresponding wave models.

Base bending moment showed a smaller shift in the reference mode but a much larger change in dispersion. Without wind, the most probable extreme increased from 4678 to 4962 kN m, approximately 6.1 percent, while the fitted standard deviation increased from 637 to 1281 kN m. With wind, the most probable extreme increased from 4590 to 5154 kN m, approximately 12.3 percent. The isolated wind effect on

the modal base moment was $(4590 - 4678)/4678 = -1.9\%$ in the linear case and $(5154 - 4962)/4962 = +3.9\%$ in the second-order case, because the elevation of the aerodynamic resultant affects moment more than shear [42].

The 3600 s estimator comparison in Figure 7 shows that Weibull-3PKU, Weibull-POT, and Weibull-POT-L-moment were closest to the reported references. Weibull-L-moment and Hermite-L-moment substantially overestimated the nonlinear moment and exhibited large spread. This result is important because an estimator that performs well for one response quantity need not perform equally well for another; distribution selection should therefore be response-specific and supported by predictive diagnostics [42].

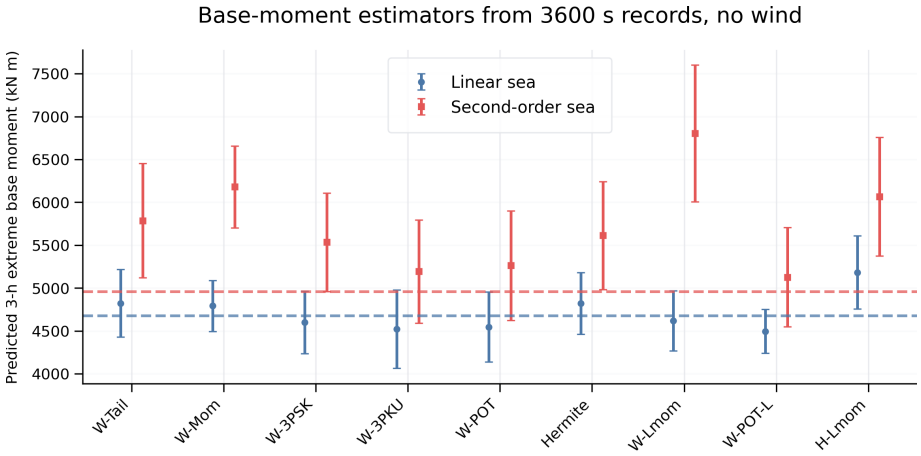


Fig. 7 Base-moment extreme estimates from 3600 s records without wind. Dashed lines indicate the three-hour Gumbel reference values.

A final sensitivity analysis increased H_s from 5.5 to 7.5 m, changed T_p from 13 to 14 s, and considered a 25 m/s wind while retaining the current. Figure 8 uses the Weibull-POT estimator to display the reported response. Base shear increased from 556.9/734.0 kN in the baseline linear/second-order cases to 985.8/1523.7 kN in the severe case with wind. Base moment increased from 4547/5262 kN m to 7718/9332 kN m. The severe environment therefore amplified both the absolute demand and the separation between linear and second-order predictions [42].

Taken together, the results support four engineering conclusions: First, 600 s records were inadequate for stable three-hour extreme prediction in this application. Second, second-order wave modelling affected base shear more strongly than top displacement and increased variability for all principal responses. Third, no single estimator dominated for every response, although three-parameter Weibull and POT-based variants were consistently competitive. Fourth, severe sea-state parameters increased the practical significance of nonlinear wave modelling, making model-form uncertainty comparable with or larger than differences among statistical estimators [42].

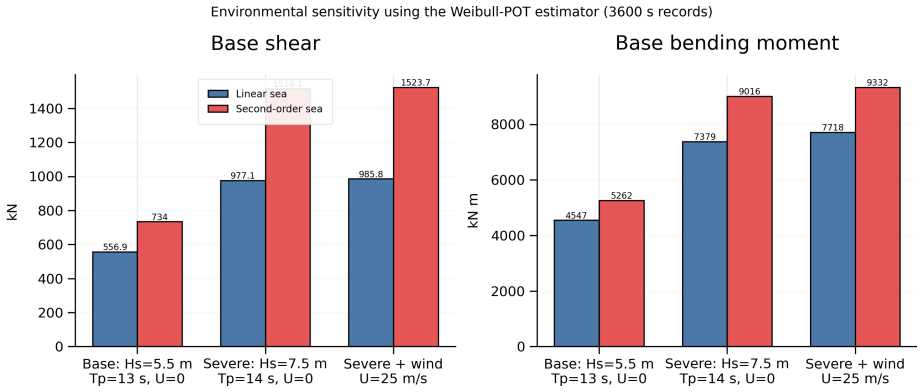


Fig. 8 Environmental sensitivity of base shear and base moment using the reported Weibull-POT estimates from 3600 s records.

22 International extensions beyond the reference methodology

Its combination of second-order potential theory, time-domain structural analysis, and non-Gaussian extreme estimation remains technically valuable, but an international application should place the short-term simulations inside a longer-term metocean and reliability framework. Recent work on fully probabilistic offshore response emphasizes forward simulation of the joint environment and structural response rather than assuming that one environmental contour point is necessarily governing [13, 43].

A first improvement is to replace isolated distribution selection by an ensemble workflow. Weibull, Hermite, GEV, and GPD models can be retained as candidates, but predictive performance should be compared by blocked cross-validation or leave-one-storm-out validation. Model uncertainty can then be propagated through Bayesian model averaging or stacking rather than suppressed by selecting a single best fit. This is especially useful when only twenty three-hour maxima are available, because the shape parameter of a tail model is weakly identified.

A second improvement is a hierarchical POT model. Threshold exceedances from multiple realizations can be pooled while allowing sea-state-specific random effects. A Poisson occurrence process describes the number of independent exceedance clusters, and a GPD describes excess magnitude. Bayesian POT methods are attractive when sampling variability is large because posterior intervals carry threshold, rate, and tail-parameter uncertainty into the response quantile [44, 46].

A third improvement is to model dependence among top displacement, base shear, and base moment. These responses are generated by the same environmental realization and should not be assigned independent design maxima. A multivariate conditional-extremes or copula model can estimate the probability that one quantity is extreme when another is large. Such a model is more informative than three unrelated univariate fits when the design limit state combines displacement and stress demand.

A fourth improvement is a nonstationary formulation when wind speed, wave height, period, or current changes across a storm. The original stationary three-hour

representation is appropriate for a short-term benchmark, but long-term reliability should condition response parameters on the evolving environment. A storm-based hierarchical model can combine within-storm simulation, annual occurrence rates, and epistemic uncertainty in hydrodynamic and damping coefficients.

Finally, surrogate models and importance sampling can reduce the number of expensive nonlinear simulations. Gaussian-process emulators, polynomial chaos, or neural surrogates should only be introduced after physics-based verification and should be trained on paired linear and second-order simulations. Importance sampling should target combinations that contribute most to failure probability, while preserving an auditable link to the governing time-domain model.

23 Conclusions and Recommendations

The conclusions reconnect the full causal numerical procedure rather than treating the chapters as independent modules. Environmental assumptions, nonlinear kinematics, load construction, structural filtering, and extreme inference must all be credible for the final design quantity to be credible.

The principal recommendation is therefore evidence-based escalation: begin with verified linear benchmarks, add second-order physics where depth and steepness require it, and increase statistical sophistication only when the available sample supports the additional parameters.

The paper has established a sequential and equation-based framework for environmental simulation, loading, dynamic response, and extreme-value analysis of slender offshore structures. The formulation distinguishes direct spectral recurrence from a true IFFT, linear from second-order kinematics, fixed-member from moving-member Morison loading, physical-coordinate from modal integration, and conventional moments from L-moments and tail estimators.

A credible application requires four forms of closure: physical closure through consistent units and force definitions; numerical closure through convergence and equilibrium; statistical closure through ensemble uncertainty; and documentary closure through reproducible inputs and assumptions. No source-code listing is required for this purpose, but every computational branch must map to a stated equation and test.

The recommended workflow is to verify each module on analytical cases, validate loads and modal properties independently, perform temporal and spatial refinement, quantify coefficient and environmental uncertainty, and only then compare extreme estimators. This sequence prevents statistical sophistication from compensating for errors in the underlying mechanics.

References

References

[1] API (2000). *API RP 2A-WSD*, 21st ed.

[2] Agarwal, P., and Manuel, L. (2009). Nonlinear waves for long-term loads. *J. Offshore Mech. Arct. Eng.* 131(3), 031601.

[3] Agarwal, P., and Manuel, L. (2010). Irregular nonlinear waves in coupled simulation. AIAA 2010-996.

[4] Alves, J. H. G. M., Banner, M. L., and Young, I. R. (2003). Revisiting PM asymptotics. *J. Phys. Oceanogr.* 33, 1301–1323.

[5] Bathe, K.-J. (1996). *Finite Element Procedures*. Prentice Hall.

[6] Cartwright, D. E., and Longuet-Higgins, M. S. (1956). Distribution of maxima of a random function. NIO Report.

[7] Chakrabarti, S. K. (1987). *Hydrodynamics of Offshore Structures*. Springer/WIT.

[8] Clough, R. W., and Penzien, J. (1993). *Dynamics of Structures*. McGraw–Hill.

[9] Davenport, A. G. (1967). The dependence of wind loads on meteorological parameters. *Proc. Int. Research Seminar on Wind Effects on Buildings and Structures*, Ottawa, Canada, 11–15 September 1967, Vol. 1, 19–82. University of Toronto Press, 1968.

[10] Dean, R. G., and Dalrymple, R. A. (1991). *Water Wave Mechanics for Engineers and Scientists*. World Scientific.

[11] Deaves, D., and Harris, R. (1978). A mathematical model of the structure of strong winds. *Report*, Building Research Establishment.

[12] DNV GL (2014). *DNV-RP-C205: Environmental Conditions and Environmental Loads*.

[13] DNV (2025). *DNV-RP-C205*, April 2025 edition.

[14] Elfouhaily, T., Chapron, B., Katsaros, K., and Vandemark, D. (1997). A unified directional spectrum for wind-driven waves. *J. Geophys. Res.* 102(C7), 15781–15796.

[15] Embrechts, P., Klüppelberg, C., and Mikosch, T. (1997). *Modelling Extremal Events*. Springer.

[16] Faltinsen, O. M. (1990). *Sea Loads on Ships and Offshore Structures*. Cambridge Univ. Press.

[17] Goda, Y. (2010). *Random Seas and Design of Maritime Structures*. World Scientific.

[18] Harris, R. I. (1978). On the spectrum of gustiness in high winds.

[19] Hasselmann, K., et al. (1973). Measurements during JONSWAP. *Erg. zur Dtsch. Hydrogr. Z.*, A(8).

[20] Haver, S., and Winterstein, S. R. (2009). Environmental contour lines: estimating long-term extremes. *Trans. SNAME* 116, 116–127.

[21] Haver, S., Bruserud, K., and Baarholm, G. S. (2013). Environmental contour method: approximate design extremes. Wave Workshop paper.

[22] Hilber, H. M., Hughes, T. J. R., and Taylor, R. L. (1977). Improved numerical dissipation for time integration. *Earthquake Eng. Struct. Dyn.* 5(3), 283–292.

[23] Holthuijsen, L. H. (2010). *Waves in Oceanic and Coastal Waters.* Cambridge Univ. Press.

[24] Hosking, J. R. M. (1990). L-moments: analysis and estimation of distributions. *JRSS-B* 52(1), 105–124.

[25] Kaimal, J. C., et al. (1972). Spectral characteristics of surface-layer turbulence. *QJRMS* 98(417), 563–589.

[26] Longuet-Higgins, M. S. (1952,1953). Statistical distribution of sea wave heights. *J. Mar. Res.* 11(3), 245–266.

[27] Longuet-Higgins, M. S. (1957). The statistical analysis of a random, moving surface. *Phil. Trans. R. Soc. A* 249, 321–387.

[28] Morison, J. R., Johnson, J. W., and Schaaf, S. A. (1950). The force exerted by surface waves on piles. *J. Petrol. Technol.* 2(5), 149–154.

[29] Newmark, N. M. (1959). A method of computation for structural dynamics. *ASCE J. Eng. Mech. Div.* 85(EM3), 67–94.

[30] Nascimento, L. S. A. (2009). *Análise de Valores Extremos de Parâmetros de Resposta Dinâmica de Plataformas Auto-Elevatórias.* M.Sc. Dissertation, COPPE/UFRJ.

[31] Nascimento, L. S. A., Sagrilo, L. V. S., and Ellwanger, G. B. (2011). On the extreme value analysis of jack-up dynamic response parameters. *Marine Systems & Ocean Technology*, 6(2), 75–86.

[32] Nascimento, L. S. A., Sagrilo, L. V. S., and Ellwanger, G. B. (2012). Conventional and Linear Statistical Moments Applied in Extreme Value Analysis of Non-Gaussian Response of Jack-Ups. *Proc. OMAE2012*, Paper OMAE2012-83583.

[33] Nascimento, L. S. A., Sagrilo, L. V. S., and Ellwanger, G. B. (2017). Extreme Value Analyses of Dynamic Response Parameters of a Wind Tower Structure Under Short-Term Nonlinear Irregular Seastate. *Proc. OMAE2017*, Paper OMAE2017-61495.

[34] Ochi, M. K. (1998). *Ocean Waves: The Stochastic Approach*. Cambridge Univ. Press.

[35] Pickands, J. (1975). Statistical inference using extreme order statistics. *Ann. Stat.* 3(1), 119–131.

[36] Pierson, W. J., and Moskowitz, L. (1964). A proposed spectral form for fully developed wind seas. *J. Geophys. Res.* 69(24), 5181–5190.

[37] Rice, S. O. (1944). Mathematical analysis of random noise. *Bell Syst. Tech. J.* 23, 282–332.

[38] Shinozuka, M., and Deodatis, G. (1991). Simulation by spectral representation. *Appl. Mech. Rev.* 44(4), 191–204.

[39] Sumer, B. M., and Fredsøe, J. (1997). *Hydrodynamics Around Cylindrical Structures*. World Scientific.

[40] Winterstein, S. R. (1988). Nonlinear vibration models for extremes and fatigue. *J. Eng. Mech.* 114(10), 1772–1790.

[41] Winterstein, S. R., and MacKenzie, C. A. (2013). Extremes of nonlinear vibration. *J. Offshore Mech. Arct. Eng.* 135(2), 021602.

[42] Nascimento, L.S., 2016. Análise Estatística de Respostas Dinâmicas de Estruturas Tubulares sob Carregamento de Onda Irregular Não Linear. Doctoral thesis, COPPE/UFRJ, Rio de Janeiro.

[43] Speers, M., Randell, D., Tawn, J., Jonathan, P., 2024. Estimating metocean environments associated with extreme structural response to demonstrate the dangers of environmental contour methods. *Ocean Engineering* 311, 118754. https://doi.org/10.1016/j.oceaneng.2024.118754.

[44] Chiodo, E., De Angelis, F., Diban, B., Mazzanti, G., 2023. Bayes inference of structural safety under extreme wind loads based upon a peak-over-threshold process of exceedances. Mathematical and Computational Applications 28(6), 111.

[45] Sharma, J.N., Dean, R.G., 1981. Second-order directional seas and associated wave forces. Society of Petroleum Engineers Journal 21(1), 129–140. https://doi.org/10.2118/8584-PA.

[46] Coles, S., 2001. An Introduction to Statistical Modeling of Extreme Values. Springer, London. https://doi.org/10.1007/978-1-4471-3675-0.

[47] Hosking, J.R.M., Wallis, J.R., 1997. Regional Frequency Analysis: An Approach Based on L-Moments. Cambridge University Press, Cambridge.

[48] IEC, 2019. IEC 61400-3-1:2019, Wind energy generation systems - Part 3-1: Design requirements for fixed offshore wind turbines. International Electrotechnical Commission, Geneva.

[49] Ross, E., Astrup, O.C., Bitner-Gregersen, E., Bunn, N., Feld, G., Gouldby, B., Huseby, A., Liu, Y., Randell, D., Vanem, E., Jonathan, P., 2020. On environmental contours for marine and coastal design. Ocean Engineering 195, 106194.

[50] Mu, J., Shi, W., Cao, L., Shang, J., Han, X., Yang, Y., Liu, L., Cheng, G., 2026. Effects of second-order wave forces on the extreme response estimation of a TLP offshore wind turbine under multi-directional wind-wave loads. Journal of Marine Science and Engineering 14, 921.

[51] Wiener, N. (1930). Generalized harmonic analysis. *Acta Mathematica* 55, 117–258. https://doi.org/10.1007/BF02546511.

[52] Airy, G. B. (1845). Tides and waves. *Encyclopaedia Metropolitana*, vol. 5, 241–396.

[53] Babanin, A. (2011). *Breaking and Dissipation of Ocean Surface Waves*. Cambridge University Press.

[54] Balkema, A. A., and de Haan, L. (1974). Residual life time at great age. *Ann. Probab.* 2, 792–804.

[55] Bathe, K.-J., and Wilson, E. L. (1976). *Numerical Methods in Finite Element Analysis*. Prentice–Hall.

[56] Beirlant, J., Goegebeur, Y., Segers, J., and Teugels, J. (2004). *Statistics of Extremes: Theory and Applications*. Wiley.

[57] Bendat, J. S., and Piersol, A. G. (2010). *Random Data: Analysis and Measurement Procedures*, 4th ed. Wiley.

[58] Benjamin, T. B., and Feir, J. E. (1967). The disintegration of wave trains on deep water. *J. Fluid Mech.* 27, 417–430.

[59] Butcher, J. C. (2008). *Numerical Methods for Ordinary Differential Equations*, 2nd ed. Wiley.

[60] Castillo, E. (1988). *Extreme Value Theory in Engineering*. Academic Press.

[61] Chopra, A. K. (2012). *Dynamics of Structures*, 4th ed. Prentice Hall.

[62] Cooley, J. W., and Tukey, J. W. (1965). An algorithm for the machine calculation of complex Fourier series. *Math. Comp.* 19, 297–301.

[63] Crandall, S. H., and Mark, W. D. (1963). *Random Vibration in Mechanical Systems*. Academic Press.

[64] Dalzell, J. F. (1999). A note on finite depth second-order wave–wave interactions. *Appl. Ocean Res.* 21, 105–111.

[65] Davenport, A. G. (1961). The spectrum of horizontal gustiness near the ground in high winds. *Q. J. R. Meteorol. Soc.* 87, 194–211.

[66] Davison, A. C., and Smith, R. L. (1990). Models for exceedances over high thresholds. *J. R. Stat. Soc. B* 52, 393–442.

[67] Ditlevsen, O. (1981). *Uncertainty Modeling*. McGraw–Hill.

[68] Donelan, M. A., Hamilton, J., and Hui, W. H. (1985). Directional spectra of wind-generated waves. *Phil. Trans. R. Soc. A* 315, 509–562.

[69] Dyrbye, C., and Hansen, S. O. (1997). *Wind Loads on Structures*. Wiley.

[70] Ewins, D. J. (2000). *Modal Testing: Theory, Practice and Application*, 2nd ed. Research Studies Press.

[71] Fenton, J. D. (1990). Nonlinear wave theories. In *The Sea*, vol. 9 (B. Le Méhauté and D. M. Hanes, eds.). Wiley.

[72] Fisher, R. A., and Tippett, L. H. C. (1928). Limiting forms of the frequency distribution of the largest or smallest member of a sample. *Proc. Cambridge Phil. Soc.* 24, 180–190.

[73] Forristall, G. Z. (1978). On the statistical distribution of wave heights in a storm. *J. Geophys. Res.* 83, 2353–2358.

[74] Forristall, G. Z. (2000). Wave crest distributions: observations and second-order theory. *J. Phys. Oceanogr.* 30, 1931–1943.

[75] Géradin, M., and Rixen, D. (1997). *Mechanical Vibrations: Theory and Application to Structural Dynamics*. Wiley.

[76] Gnedenko, B. V. (1943). Sur la distribution limite du terme maximum d'une série aléatoire. *Ann. Math.* 44, 423–453.

[77] Greenwood, J. A., Landwehr, J. M., Matalas, N. C., and Wallis, J. R. (1979). Probability weighted moments: definition and relation to parameters of several distributions expressible in inverse form. *Water Resour. Res.* 15, 1049–1054.

[78] Grigoriu, M. (1995). *Applied Non-Gaussian Processes*. Prentice Hall.

[79] Gumbel, E. J. (1958). *Statistics of Extremes*. Columbia University Press.

[80] Hairer, E., Nørsett, S. P., and Wanner, G. (1993). *Solving Ordinary Differential Equations I*, 2nd ed. Springer.

[81] Harris, R. I. (1971). The nature of the wind. In *Proc. Seminar on the Modern Design of Wind-Sensitive Structures*, Institution of Civil Engineers, London.

[82] Hasselmann, K. (1962). On the non-linear energy transfer in a gravity-wave spectrum. *J. Fluid Mech.* 12, 481–500.

[83] Hughes, T. J. R. (1987). *The Finite Element Method*. Prentice–Hall.

[84] Keulegan, G. H., and Carpenter, L. H. (1958). Forces on cylinders and plates in an oscillating fluid. *J. Res. Nat. Bur. Stand.* 60, 423–440.

[85] Komen, G. J., Hasselmann, S., and Hasselmann, K. (1984). On the existence of a fully developed wind-sea spectrum. *J. Phys. Oceanogr.* 14, 1271–1285.

[86] Kotz, S., and Nadarajah, S. (2000). *Extreme Value Distributions*. Imperial College Press.

[87] Lamb, H. (1932). *Hydrodynamics*, 6th ed. Cambridge University Press.

[88] Leadbetter, M. R., Lindgren, G., and Rootzén, H. (1983). *Extremes and Related Properties of Random Sequences and Processes*. Springer.

[89] Lighthill, J. (1978). *Waves in Fluids*. Cambridge University Press.

[90] Longuet-Higgins, M. S. (1963). The effect of non-linearities on statistical distributions in the theory of sea waves. *J. Fluid Mech.* 17, 459–480.

[91] Longuet-Higgins, M. S., and Stewart, R. W. (1964). Radiation stresses in water waves; a physical discussion, with applications. *Deep-Sea Res.* 11, 529–562.

[92] Lutes, L. D., and Sarkani, S. (1997). *Random Vibrations: Analysis of Structural and Mechanical Systems*. Butterworth–Heinemann.

[93] Madsen, H. O., Krenk, S., and Lind, N. C. (1986). *Methods of Structural Safety*. Prentice–Hall.

[94] Mei, C. C. (1989). *The Applied Dynamics of Ocean Surface Waves*. World Scientific.

[95] Meirovitch, L. (2001). *Fundamentals of Vibrations*. McGraw–Hill.

[96] Melchers, R. E. (1999). *Structural Reliability Analysis and Prediction*, 2nd ed. Wiley.

[97] Melville, W. K. (1996). The role of surface-wave breaking in air–sea interaction. *Ann. Rev. Fluid Mech.* 28, 279–321.

[98] Miche, R. (1944). Mouvements ondulatoires de la mer en profondeur constante ou décroissante. *Annales des Ponts et Chaussées*, 25–78, 131–164, 270–292, 369–406.

[99] Mitsuyasu, H., Tasai, F., Suhara, T., Mizuno, S., Ohkusu, M., Honda, T., and Rikiishi, K. (1975). Observations of the directional spectrum of ocean waves using a cloverleaf buoy. *J. Phys. Oceanogr.* 5, 750–760.

[100] Mori, N., and Janssen, P. A. E. M. (2006). On kurtosis and occurrence probability of freak waves. *J. Phys. Oceanogr.* 36, 1471–1483.

[101] Naess, A. (1985). Statistical analysis of second-order response of marine structures. *J. Ship Res.* 29, 270–284.

[102] Naess, A., and Moan, T. (2013). *Stochastic Dynamics of Marine Structures*. Cambridge University Press.

[103] Newland, D. E. (1993). *An Introduction to Random Vibrations, Spectral and Wavelet Analysis*, 3rd ed. Longman.

[104] Newman, J. N. (1980). *Marine Hydrodynamics*. MIT Press.

[105] Ochi, M. K., and Shin, Y. S. (1988). Wind turbulent spectra for design consideration of offshore structures. *Proc. 20th Offshore Technol. Conf. (OTC)*, OTC 5737.

[106] Onorato, M., Osborne, A. R., Serio, M., and Bertone, S. (2001). Freak waves in random oceanic sea states. *Phys. Rev. Lett.* 86, 5831–5834.

[107] Papoulis, A. (1991). *Probability, Random Variables, and Stochastic Processes*, 3rd ed. McGraw–Hill.

[108] Phillips, O. M. (1958). The equilibrium range in the spectrum of wind-generated waves. *J. Fluid Mech.* 4, 426–434.

[109] Phillips, O. M. (1977). *The Dynamics of the Upper Ocean*, 2nd ed. Cambridge University Press.

[110] Priestley, M. B. (1981). *Spectral Analysis and Time Series*. Academic Press.

[111] Rice, S. O. (1945). Mathematical analysis of random noise (concluded). *Bell Syst. Tech. J.* 24, 46–156.

[112] Sarpkaya, T. (1976). Vortex shedding and resistance in harmonic flow about smooth and rough circular cylinders at high Reynolds numbers. Report NPS-59SL76021, Naval Postgraduate School, Monterey.

[113] Sarpkaya, T. (2010). *Wave Forces on Offshore Structures*. Cambridge University Press.

[114] Sarpkaya, T., and Isaacson, M. (1981). *Mechanics of Wave Forces on Offshore Structures*. Van Nostrand Reinhold.

[115] Shinozuka, M. (1971). Simulation of multivariate and multidimensional random processes. *J. Acoust. Soc. Am.* 49, 357–367.

[116] Shinozuka, M., and Jan, C.-M. (1972). Digital simulation of random processes and its applications. *J. Sound Vib.* 25, 111–128.

[117] Simiu, E., and Scanlan, R. H. (1996). *Wind Effects on Structures*, 3rd ed. Wiley.

[118] Solari, G. (1987). Turbulence modeling for gust loading. *J. Struct. Eng.* 113, 1550–1569.

[119] Stokes, G. G. (1847). On the theory of oscillatory waves. *Trans. Cambridge Phil. Soc.* 8, 441–455.

[120] Tayfun, M. A. (1980). Narrow-band nonlinear sea waves. *J. Geophys. Res.* 85, 1548–1552.

[121] Thoft-Christensen, P., and Baker, M. J. (1982). *Structural Reliability Theory and Its Applications*. Springer.

[122] Tucker, M. J., and Pitt, E. G. (2001). *Waves in Ocean Engineering*. Elsevier.

[123] Ursell, F. (1953). The long-wave paradox in the theory of gravity waves. *Proc. Cambridge Phil. Soc.* 49, 685–694.

[124] Vanmarcke, E. (1983). *Random Fields: Analysis and Synthesis*. MIT Press.

[125] WAMDI Group (1988). The WAM model—a third generation ocean wave prediction model. *J. Phys. Oceanogr.* 18, 1775–1810.

[126] Weibull, W. (1951). A statistical distribution function of wide applicability. *J. Appl. Mech.* 18, 293–297.

[127] Wheeler, J. D. (1970). Method for calculating forces produced by irregular waves. *J. Petrol. Technol.* 22, 359–367.

[128] Whitham, G. B. (1974). *Linear and Nonlinear Waves*. Wiley.

[129] Wood, W. L. (1990). *Practical Time-Stepping Schemes*. Oxford University Press.

[130] Young, I. R. (1999). *Wind Generated Ocean Waves*. Elsevier.

[131] Zakharov, V. E. (1968). Stability of periodic waves of finite amplitude on the surface of a deep fluid. *J. Appl. Mech. Tech. Phys.* 9, 190–194.

[132] Zienkiewicz, O. C., and Taylor, R. L. (2000). *The Finite Element Method*, 5th ed. Butterworth–Heinemann.

[133] Kolmogorov, A. N. (1933). *Grundbegriffe der Wahrscheinlichkeitsrechnung.* Springer.

[134] Le Méhauté, B. (1976). *An Introduction to Hydrodynamics and Water Waves.* Springer.

[135] Ochi, M. K., and Hubble, E. N. (1976). Six-parameter wave spectra. *Proc. 15th Coastal Eng. Conf.*, ASCE, 301–328.

Declarations

Funding This research received no specific grant from any funding agency in the public, commercial, or not-for-profit sectors.
Competing interests The author declares no competing interests.
Ethics approval Not applicable.
Consent to participate Not applicable.
Consent for publication Not applicable.
Data availability All data generated or analysed during this study are included in this published article. The case-study data are reproduced from the published numerical investigation cited in the text.
Code availability The GERASINAL program used for the simulations is the author's research code and is available from the corresponding author on reasonable request.
Author contributions L. S. do Nascimento is the sole author and is responsible for the conceptualization, methodology, analysis, and writing of this manuscript.